Ore Geology Reviews 78 (2016) 371–387

Contents lists available at ScienceDirect

Ore Geology Reviews

journal homepage: www.elsevier.com/locate/oregeorev

# The Nadun Cu–Au mineralization, central Tibet: Root of a high sulfidation epithermal deposit

Jin-Xiang Li [a,b,*], Ke-Zhang Qin [b,c], Guang-Ming Li [b,c], Noreen J. Evans [d], Jun-Xing Zhao [c], Ming-Jian Cao [c], Fang Huang [e]

[a] Key Laboratory of Continental Collision and Plateau Uplift, Institute of Tibetan Plateau Research, Chinese Academy of Sciences, Beijing 100101, PR China
[b] CAS Center for Excellence in Tibetan Plateau Earth Sciences, Beijing 100101, PR China
[c] Key Laboratory of Mineral Resources, Institute of Geology and Geophysics, Chinese Academy of Sciences, Beijing 100029, PR China
[d] John de Laeter Center, TIGeR, Applied Geology, Curtin University, Perth, WA 6945, Australia
[e] CAS Key Laboratory of Crust-Mantle Materials and Environments, School of Earth and Space Sciences, University of Science and Technology of China, Heifei 230026, PR China

ARTICLE INFO

*Article history:*
Received 10 August 2015
Received in revised form 17 April 2016
Accepted 21 April 2016
Available online 25 April 2016

*Keywords:*
Zircon U–Pb ages
Fluid inclusions
H–O–Fe–S isotopes
Epithermal mineralization
Tibet

ABSTRACT

A new high sulfidation epithermal Cu–Au occurrence (Nadun) has been discovered adjacent to the Cretaceous Duolong porphyry Cu–Au deposit within the Bangong–Nujiang metallogenic belt, central Tibet. The Nadun Cu–Au mineralization is hosted in a tectonic–hydrothermal breccia with advanced argillic alteration, which occurs above sandstone, associated with quartz–pyrite veins. The granodiorite porphyry with strong argillic alteration yields a zircon U–Pb age of 119.1 ± 1.3 Ma, whereas the weakly argillic granodiorite porphyry intruded into the breccia has a younger age of 116.1 ± 1.3 Ma. This indicates that Cu–Au epithermal mineralization likely occurred between ~116 Ma and ~119 Ma, consistent with the duration of magmatic–hydrothermal activity at Duolong (~115–118 Ma), and providing evidence that Nadun and Duolong were formed during the same event. Moreover, the Nadun and Duolong porphyries have similar Hf isotopic compositions (εHf(t) values ranging from −8.8 to 8.1; mean = 5.0 ± 1.1, n = 32), likely indicating that the deposits are comagmatic. In addition, boiling assemblages in vapor-rich inclusions coexisting with brines occur in early stage quartz–pyrite veins, and likely record phase separation at a temperature of > 550–300 °C and pressure of 700–110 bars. Most liquid-rich fluid inclusions formed at the breccia stage show similar salinity (1.7–19.3 wt.% NaCl equiv) to vapor-rich inclusions from the underlying quartz–pyrite veins, likely indicating vapor contraction during cooling at elevated presssure. This suggests that quartz–pyrite veins may act as conduits for ore-forming fluid traveling from the porphyry to the epithermal hydrothermal system. O and H isotopic compositions ($\delta^{18}O_{fluid}$ = 0.42–9.71‰ and $\delta D$ = −102 to −66‰) suggest that ore-forming fluids are dominantly from a magmatic source with a minor addition of meteoric water at a later stage. The S and Fe isotope compositions of sulfides ($\delta^{34}S$ = −5.9 to 0.5‰ and $\delta^{57}Fe$ = −2.15 to 0.17‰) decrease from the quartz–pyrite vein to breccia ore, indicating that ore-forming fluids gradually become $SO_4^{2-}$-enriched and relatively oxidized. This body of evidence suggests that the Nadun Cu–Au mineralization may represent the root of a high sulfidation epithermal deposit.



## 1. Introduction

High sulfidation epithermal Cu–Au deposits have close spatial and temporal relationships with porphyry Cu–Au deposits in several ore districts (e.g., Hedenquist and Lowenstern, 1994; Arribas et al., 1995; Hedenquist et al., 1998; Pudack et al., 2009; Sillitoe, 2010; Chang et al., 2011; Cooke et al., 2011; Richards, 2011; Chai et al., 2014). Most geochronological, stable isotope and fluid inclusion studies have provided compelling evidence for a genetic association between them (e.g., Sillitoe, 2010; Richards, 2011). A well-known genetic model states that low density vapor-rich fluids transport Cu, Au elements from the porphyry to the epithermal environment, and subsequently contract at elevated pressure above the critical curve of the salt-water system (Heinrich et al., 2004; Heinrich, 2005; Pudack et al., 2009). There are still relatively few deposits providing evidence for this relationship, the best examples being Lepanto-Far southeast (Hedenquist et al., 1998) in the Philippines and the Maricunga belt in northern Chile (Muntean and Einaudi, 2001).

The Tibetan Plateau hosts three well known porphyry metallogenic belts (Fig. 1a, b); Gangdese, Yulong, and Bangonghu. The fist two belts host Cenozoic Cu–Mo mineralization assemblages and formed in the India-Eurasian collision setting (Hou et al., 2003, 2004), whereas the Bangonghu belt is characterized by Cu–Au mineralization assemblages and is related to Cretaceous northward subduction of the Bangong–

* Corresponding author at: Key Laboratory of Continental Collision and Plateau Uplift, Institute of Tibetan Plateau Research, Chinese Academy of Sciences, Beijing 100101, PR China.
*E-mail address:* ljx@itpcas.ac.cn (J.-X. Li).

http://dx.doi.org/10.1016/j.oregeorev.2016.04.019
0169-1368/

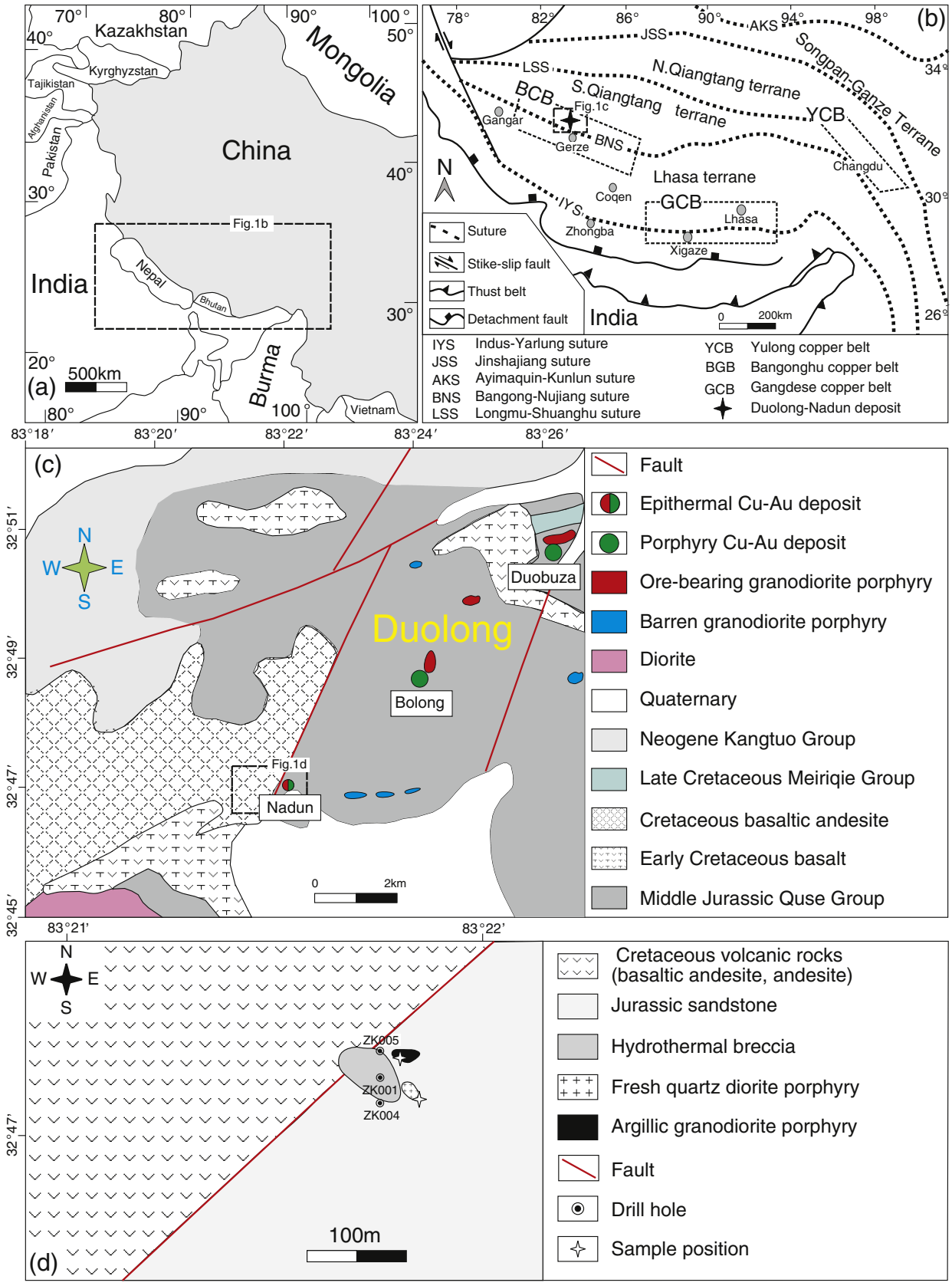


**Fig. 1.** (a) Geographic and (b) sketch tectonic map of the Himalayan–Tibetan orogen (Hou et al., 2004; Zhu et al., 2013), (c) geological and spatial map of the Duolong porphyry Cu–Au deposit and Nadun Cu–Au mineralization (Li et al., 2013, 2016), and (d) geological map of the Nadun Cu–Au mineralization (modified from Report of No. 5 Geological Team, Tibetan Bureau of Geology and Exploration, 2011), central Tibet.

Nujiang oceanic plate (Li et al., 2013). The Duolong giant Cu–Au ore district (prospective metal resources of ~25 Mt Cu and ~400 t Au) in the Bangonghu metallogenic belt is located ~100 km northwest of Gerze city (Tibet), north of the Bangong–Nujiang suture zone (BNS; Fig. 1b). The ore district covers more than 120 km$^2$ and includes several deposits including the Duolong and Naruo porphyry deposits, and the Rongna porphyry-high sulfidation epithetrmal deposit. Recently, a high sulfidation epithermal Cu–Au occurrence (Nadun; 0.14 Mt ore resources at 0.75% Cu and 1.45 g/t) was discovered in the Duolong ore district, ~1–2 km from the Cretaceous Duolong porphyry Cu–Au deposit (5.4 Mt at 0.72% Cu and 41 t at 0.23 g/t Au; Li et al., 2011b, 2013). Previous studies indicated that the ~118–115 Ma Duolong porphyry Cu–Au deposit formed in a continental arc setting from magmatic-sourced ore-forming fluids (Li et al., 2011a, 2013). However, the genesis of the Nadun deposit and its spatial, temporal, and genetic relationships with the adjacent Duolong Cu–Au deposit remain unclear. This manuscript presents new zircon U–Pb ages, fluid inclusion analysis, and H-O-Fe-S stable isotope data for the Nadun deposit. In combination with published data from the adjacent Duolong deposit, these results will be used to constrain mineralization timing and the evolution of ore-forming fluids in order to evaluate the genesis of Nadun and its genetic relationship to the Duolong deposit.

## 2. Regional geology

The Tibetan plateau consists of five terranes (from north to south: Qaidam, Kunlun, Qiangtang, Lhasa, and India), separated by four Mesozoic and Cenozoic sutures (Ayimaquin–Kunlun, Jinshajiang, Bangong–Nujiang, and Indus–Yarlung, respectively; Fig. 1a, b; Yin and Harrison, 2000; Zhu et al., 2013; Zhang et al., 2012). The Qiangtang terrane is situated in the central Tibetan plateau, bounded by the Jinshajiang suture (JSS) to the north and the Bangong–Nujiang suture (BNS) to the south (Yin and Harrison, 2000; Kapp et al., 2005). It is divided by the Mesozoic Longmu-Shuanghu suture (LSS) into a northern and a southern Qiangtang terrane (Fig. 1b; Zhang et al., 2012; Zhu et al., 2013). Additionally, the Bangong–Nujiang suture zone is characterized by a >1200-km-long east-trending belt of mainly Jurassic–Cretaceous flysch, mélange and ophiolitic fragments, and represents the remnants of the Bangong–Nujiang ocean (Yin and Harrison, 2000; Pan et al., 2012). Meanwhile, the ages of ophiolites and radiolarians indicate that the Bangong–Nujiang ocean existed at least from the Carboniferous to Early Cretaceous (Shi, 2007; Pan et al., 2012), and the Lhasa–Qiangtang collision possibly occurred at about 100 Ma (Zhang et al., 2012).

The main strata exposed in the south Qiangtang terrane consist of Carboniferous and Carboniferous–Permian sandy shale and limestone, Permian sandy slate and limestone and Jurassic clastic rock and limestone, which were intruded by the Jurassic and Cretaceous intermediate-felsic intrusions (Liu et al., 2014; Li et al., 2014). Scattered Cretaceous (120–106 Ma) arc-type volcanic rocks also occur in the southern Qiangtang terrane (Li et al., 2011b; Liu et al., 2012). Jurassic skarn Fe–Cu deposits (e.g., Fuye and Caima; Zhang et al., 2011) and Cretaceous porphyry-epithermal Cu–Au deposits (e.g., Duolong, Li et al., 2011b, 2012, 2013; Rongna, Li et al., 2015b; Qingcaoshan, Zhou et al., 2013) are associated with these intrusions in the southern Qiangtang terrane. The new discovered Nadun high sulfidation Cu–Au deposit in the Duolong ore district, which is focus of this study, is located in the southern Qiangtang terrane and at the north of the Bangong–Nujiang suture (Fig. 1b).

## 3. Ore deposit geology

The Nadun Cu–Au deposit is 1–2 km southwest of the giant Duolong porphyry Cu–Au deposit (Fig. 1c). In the Duolong-Nadun ore district, the stratigraphy comprises the Middle Jurassic Quse Group, Late Cretaceous Meiriqie Group, and Neogene Kangtuo Group (Fig. 1c). The Middle Jurassic Quse Group is a clastic-interbedded volcanic sequence of littoral facies and composed of arkosic sandstone, siltstone-interbeded siliceous rock, basalt and dacite. The Late Cretaceous Meiriqie Group contains basaltic andesite, dacite, volcanic–clastic rocks, andesite porphyry and andesite. The Neogene Kangtuo Group is composed of brown-red clay and sandy gravel (Fig. 1c). The ~118 Ma ore-forming granodiorite porphyries intruded into the Middle Jurassic Quse Group as stocks and dykes, and have contribution to the formation of the Duolong porphyry Cu–Au deposit (Li et al., 2011b, 2012, 2013). The ~118–120 Ma barren and fresh granodiorite porphyry also intruded into the Middle Jurassic Quse Group (Li et al., 2011b, 2013). The ~143 Ma Early Cretaceous basalts are pre-ore volcanic rocks, with OIB (ocean island basalts) affinities (Li et al., 2013). Syn- and post-ore Cretaceous volcanic rocks (Fig. 1c), from the Meiriqie Group, yield zircon U–Pb ages from ~118 Ma to ~105 Ma, and include basalt, basaltic andesite, and andesite with characteristics of arc magmas (Li et al., 2011b, 2016).

At the Nadun Cu–Au deposit, strongly argillic granodiorite porphyry and fresh quartz diorite porphyry intruded into the Jurassic sandstone and are exposed at the surface (Fig. 1d). Another weakly argillic granodiorite porphyry intruded into the breccia (Fig. 2). The breccia itself is hosted by Cretaceous volcanic rocks and the Jurassic Quse Group (Figs. 1d, 2), and has a length of ~100 m, width of 80 m, and vertical extension of ~180 m. Most clasts within this breccia are 3–20 cm, angular to subangular pieces of basaltic–andesitic volcanic rocks and sandsone. The breccia is matrix-supported (fine-grained rock flour; Fig. 3a, b) and cemented by quartz, carbonate, kaolinite, dickite, sulfide (Fig. 3c), and minor rutile, anhydrite, barite, and hematite. This tectonic–hydrothermal breccia was formed by a north-east strike fault and further overprinted by ore-forming fluids. Advanced argillic alteration (mainly including kaolinite, dickite, and pyrophyllite confirmed by XRD) is not extensive and only occurs locally (e.g., NDZK004-69; Fig. 3f), especially in the enargite-bearing breccia. Extensive argillic alteration (kaolinite, smectite, and illite assemblies) occurs in Cretaceous volcanic rocks, the Jurassic Quse group, and in the breccia (Figs. 2, 4a, c-f). Subordinate

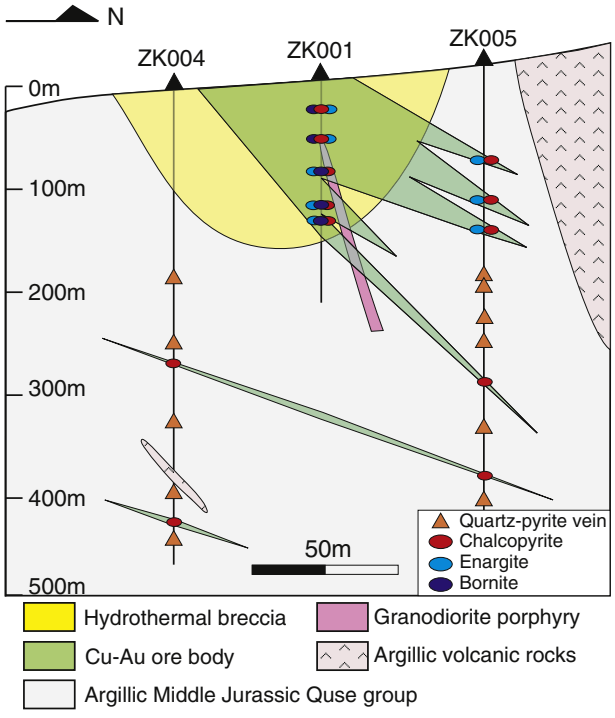


**Fig. 2.** Cross section map of the Nadun Cu–Au mineralization and Cu-bearing sulfide distribution, central Tibet. Mineralization range is from 2011 Annual Report of No. 5 Geological Team, Tibetan Bureau of Geology and Exploration.

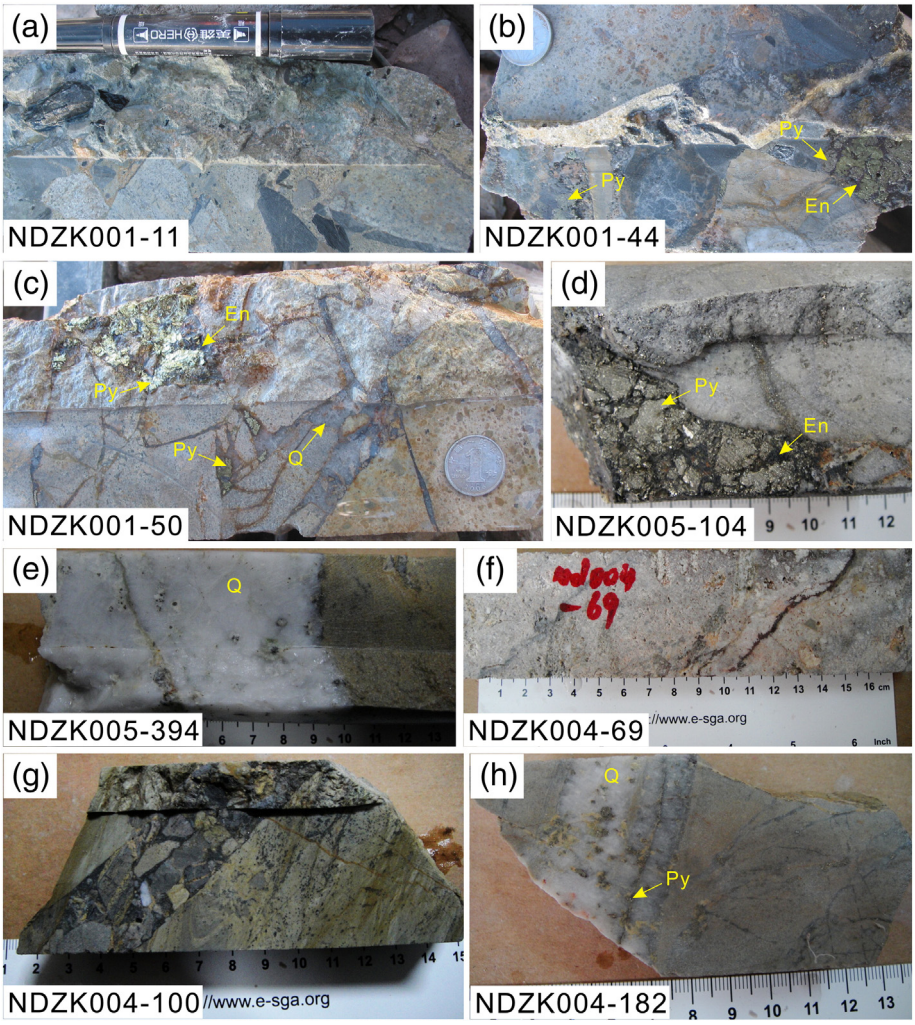


**Fig. 3.** Photographs of representative samples from Nadun Cu–Au mineralization. (a) Fine-grained rock flours matrix-supported breccia. (b, c) Tectonic–hydrothermal breccia associated with pyrite and enargite. (d) Quartz–pyrite–enargite vein with width of >1 cm, and enargite formed later than pyrite. (e) Quartz–pyrite vein (width of >6 cm) in argillic sandstone. (f) Strong argillic sandstone with fine pyrite vein. (g) Dike-like hydrothermal breccia in argillic sandstone. (h) Quartz–pyrite vein (width of 2 cm) in argillic sandstone. Abréviations: Q—quartz, Py—pyrite, En—enargite.

sericitization (fine-grained muscovite) is mainly distributed throughout the Jurassic Quse group rocks (Fig. 4c-f) and below the breccia body. Quartz–pyrite veins with sericite halos have a width of ~1–3cm and occur in the argillic Jurassic sandsone (Fig. 3e, h). Carbonatization, the last hydrothermal event, overprinted the entire alteration zone and occurs as vein-like, infilled and disseminated carbonate (Fig. 4d, f). Although alunite-bearing alteration has not been identified in this deposit, it is possible that evidence of it has been subsequently eroded. Recent exploration shows that neither potassic alteration nor an ore-forming porphyry have been discovered below Nadun. Moreover, Cu–Au mineralization is dominantly hosted by the breccia body and subordinately by quartz–pyrite–chalcopyrite ± enargite veins in argillic sandstone (ZK005-104; Fig. 3d). Cu-bearing sulfide is manifest as enargite, bornite, chalcopyrite, and digenite assemblage in upper levels and as minor chalcopyrite at depth (Fig. 2). Enargite–tennantite, bornite, chalcopyrite, and digenite commonly fill fractures in pyrite in ore breccias (Figs. 3b, d, 5a-e), suggesting that the Cu-bearing minerals formed later. Vein-like enargite–tennantite cuts and replaces early infilling chalcopyrite (Fig. 5d), indicating that enargite was formed later than chalcopyrite and bornite. Wittichenite occurs in chalcopyrite and digenite. Galena locally infills porosity in chalcopyrite in breccia ore (Fig. 5g), and occurs with sphalerite and pyrite in quartz-bearing veins hosted by argillic sandstone (Fig. 5h).

## 4. Sampling and analytical methods

### 4.1. Zircon U–Pb ages and in-situ Hf isotopes

Two argillic granodiorite porphyries (ND-1 and NDZK001-81) and one fresh quartz diorite porphyry (ND-10) were collected for zircon U–Pb geochronology and *in-situ* Hf isotope analyses. They show porphyritic textures and mainly consist of amphibole, plagioclase, quartz, K-feldspar, and minor (< 1%) apatite, magnetite, and zircon. The studied granodiorite porphyry ND-1 exposed at the surface has undergone strong argillic alteration, whereas another granodiorite porphyry NDZK001-81 intruded the mineralized breccia and underwent only weak argillic alteration.

Zircon crystals were obtained from crushed rock using a combination of heavy liquid and magnetic separation techniques. Individual crystals were hand-picked under a binocular microscope, subsequently mounted in epoxy and polished to expose the cores of the grains. The sites for zircon U–Pb age and Hf isotope analysis were selected on the

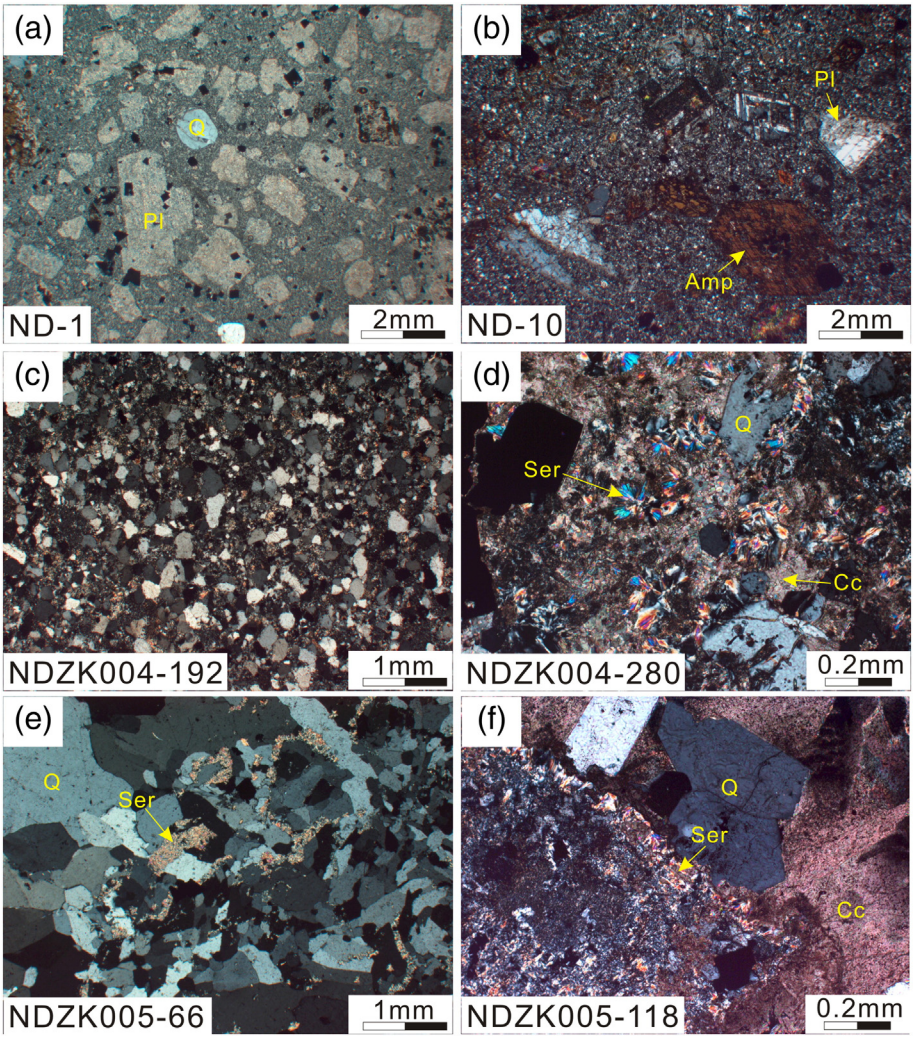


**Fig. 4.** Photographs of typical alterations from the Nadun Cu–Au mineralization. (a) Argillic granodiorite porphyry. (b) Post-ore quartz diorite porphyry. (c) Argillic sandstone. (d) Quartz–sericite–pyrite–carbonate alteration assemblages in argillic sandstone. (e) Quartz–sericite–pyrite vein in argillic sandstone. (f) Quartz–sericite–kaolinite–pyrite–carbonate alteration assemblages in argillic sandstone. Abréviations: Q—quartz, Amp—amphibole, Pl—plagioclase, Ser—sericite, Cc—carbonate.

basis of cathodoluminescence (CL) images (Fig. 6), which were obtained using a LEO1450VP scanning electron microscope (SEM) at the Institute of Geology and Geophysics, Chinese Academy of Sciences (IGGCAS), Beijing, China.

Zircon U–Pb geochronology of one granodiorite porphyry NDZK001-81 was performed in the John De Laeter Center for Isotope Research, Curtin University, using SHRIMP secondary ion mass spectrometry. The U–Pb analytical procedures have been described by Kennedy et al. (2014). A 25–30 μm diameter spot was used, with a beam of ~2–3 nA. The measured Plesovice zircon standard yielded a concordia age of 334.1 ± 1.2 Ma (n = 8; MSWD = 1.3), consistent with the published age of 337.1 ± 0.4 Ma (Slama et al., 2008). Zircon U–Pb isotopic data are listed in Supplemental Data Table 1.

Zircon U–Pb–Hf isotopic analyses of two samples ND-1 and ND-10 were conducted on a Neptune MC–ICP–MS equipped with a 193-nm laser at IGGCAS. During zircon U–Pb isotopic analyses, a laser repetition rate of 6~8 Hz at 100 mJ and spot size of 40–60 μm were used. Standard blocks (Harvard zircon 91500 (Wiedenbeck et al., 1995), GJ-1 (Jackson et al., 2004) and NIST SRM 610) were interspersed between every 5 sample analyses. Detailed analytical techniques have been described by Wu et al. (2006) and Xie et al. (2008). Common Pb contents were evaluated using the method described by Andersen (2002) while age calculations and concordia diagrams were generated using ISOPLOT (v. 3.0) (Ludwig, 2003). Uncertainties for individual analyses (ratios and ages) are quoted at the 1σ level, whereas the errors on concordia and weighted mean ages are quoted at the 2σ level. Zircon U–Pb isotopic data are listed in Supplemental Data Table 2.

Zircon Hf isotope analyses were conducted on the same zircon grains that were previously analyzed for U–Pb ages. A $^{176}Hf/^{177}Hf$ isotopic ratio of 0.282300 is recommended as the standard value for 91500 (Wu et al., 2006), and is used to correct Hf isotopic measurements. Detailed analytical techniques have been described by Wu et al. (2006) and Xie et al. (2008). Zircon standard GJ-1, treated as an unknown, sample yielded a weighted $^{176}Hf/^{177}Hf$ ratio of 0.282013 ± 0.000009 (2σ, n = 18), consistent with the recommended Hf isotopic ratio (0.282000 ± 0.000005, Morel et al., 2008). Initial $^{176}Hf/^{177}Hf$ is calculated according to the corresponding spot age, and the value of εHf(t) is calculated relative to the chondritic reservoir ($^{176}Hf/^{177}Hf$ ratio of 0.282785 and $^{176}Lu/^{177}Hf$ of 0.0336; Bouvier et al., 2008). Single-stage Hf model ages ($T_{DM}$) are calculated relative to the depleted mantle which is assumed to have a linear isotopic growth from $^{176}Hf/^{177}Hf = 0.279718$ at 4.55Ga to 0.283250 at present, with a $^{176}Lu/^{177}Hf$ ratio of 0.0384 (Vervoort and Blichert-Toft, 1999; Griffin et al., 2000). Two-stage Hf

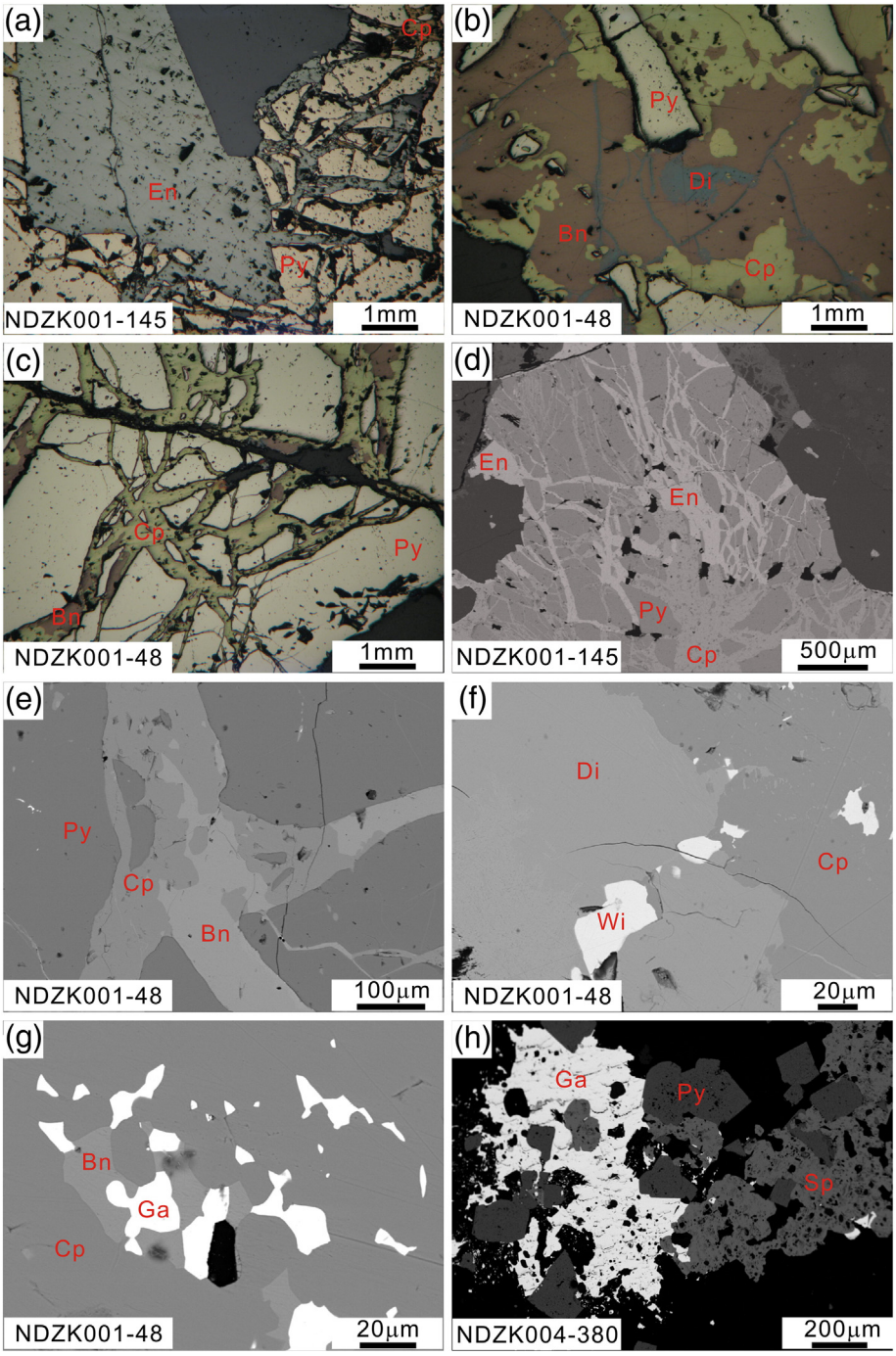


**Fig. 5.** Photographic and BSE photos of typical sulfides from the Nadun Cu–Au mineralization. (a) Pyrite is broken and infilled by enargite and chalcopyrite in breccia. (b) Chalcopyrite–bornite–digenite assemblages form later than pyrite. (c) Bornite and chalcopyrite fill fractures in pyrite. (d) Enargite infill broken pyrite and cut early chalcopyrite. (e) Pyrite is broken and infilled by bornite and chalcopyrite in breccia. (f) Chalcopyrite, digenite, and wittichenite in breccia. (g) Chalcopyrite, bornite, and galena in breccia. (h) Galena–sphalerite–pyrite assemblages in quartz-bearing vein hosted by argillic sandstone. Abbreviations: Py—pyrite, En—enargite, Bn—bornite, Sp—sphalerite, Cp—chalcopyrite, Di—digenite, Ga—galena, Wi—wittichenite.

model ages ($T^{C}_{DM}$) are calculated by assuming a mean $^{176}Lu/^{177}Hf$ value of 0.015 for the average continental crust (Griffin et al., 2002). Zircon Hf isotopic data are listed in Supplemental Data Table 3.

### 4.2. Sulfide compositions by EMPA

Compositions of sulfides were determined from representative breccia ore samples at the Analytical Laboratory Beijing Research Institute of Uranium Geology (ALBRIUG), China, using a JEOL JXA-8100 electron microprobe analyzer (EMPA). The measured sample sections were carbon coating and placed into the electron microprobe vacuum chamber. The operating conditions were 15 kV accelerating voltage, $1 \times 10^{-8}$ A beam current, and 5μm beam spot. Pure elements and minerals, including pyrite, chalcopyrite, galena, sphalerite, stibnite and synthetic GaAs were used as standards. The detection limits for the target elements are: As 0.03%, Sn 0.03%, Ag 0.02%, S 0.02%, Fe 0.03%, Cu 0.05%, Bi 0.08%, Pb 0.04%, Cd 0.03%, Zn 0.05%, Sb 0.04%, Te 0.03%, Ni 0.02%, Co 0.03%, Mn 0.01%, and Sn 0.03%.

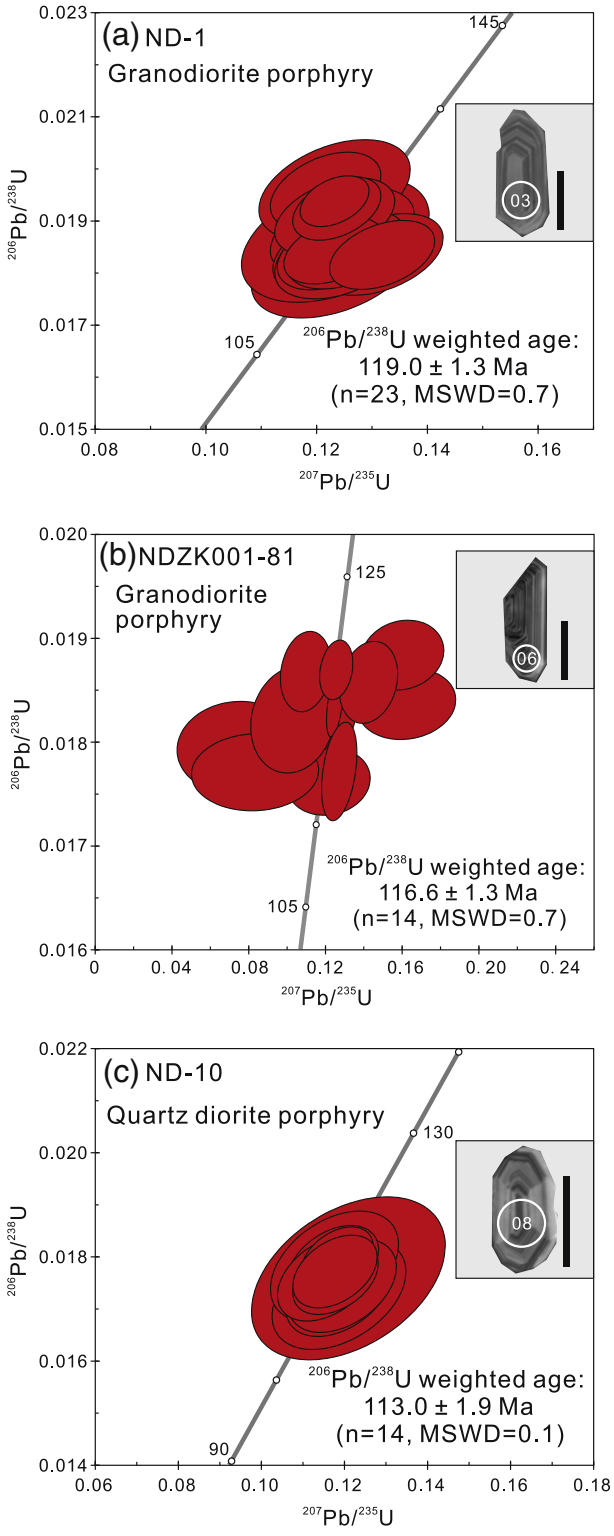


**Fig. 6.** U–Pb concordia diagrams, weighted mean ages, and representative cathodoluminescence (CL) images of zircons from granodiorite porphyries (a, b) and quartz diorite porphyry (c) in the Nadun Cu–Au mineralization. Scale bars are 100 μm.

### 4.3. Fluid inclusions

Doubly polished thin sections were prepared from seven quartz–pyrite veins and four from breccias. Microthermometric measurements were carried out using a Linkam THMSG-600 heating-freezing stage at IGGCAS. The stage was calibrated with a set of synthetic fluid inclusion standards, with precision of ±0.1 °C near or below 0 °C and ±1 °C at higher temperatures. Salinities of liqiud- and vapor-rich fluid inclusions were calculated from measured ice-melting temperatures using the equations in Hall et al. (1988). The salinity of brine inclusions is obtained using the equation of Sterner et al. (1988) for inclusions containing halite, and from the $H_2O$-NaCl-KCl diagram (Roedder, 1984) for three-phase inclusions containing halite and sylvite.

### 4.4. O and H isotopes

Oxygen and hydrogen isotope analyses were performed on the thirteen quartz samples selected from quartz–pyrite veins and breccias, using a Thermo MAT-253 stable isotope ratio mass spectrometer at ALBRIUG. The procedures for O and H isotope analyses are similar to those described by Cooke et al. (2011). All isotopic ratios are reported in the standard delta notation as per mil deviations from Vienna Standard Mean Ocean Water (V-SMOW). Precision is better than ±0.2 per mil for $\delta^{18}O$ values and ±2 per mil for δD values. The fractionation equation (Matsuhisa et al., 1979) has been used to calculate the $\delta^{18}O$ values of fluids in equilibrium with quartz.

### 4.5. S and Fe isotopes

Sulfides were collected from tectonic–hydrothermal breccia ore and quartz–pyrite veins in the Nadun mineralization (Table 4). Twenty-seven sulfides (pyrite, chalcopyrite, bornite, and enargite) were selected for S isotope analyses using a Finnigan MAT 251 mass spectrometer at the Analytical Laboratory Beijing Research Institute of Uranium Geology (ALBRIUG), China. Results are reported in $\delta^{34}S$ notation relative to the Vienna Canyon Diablo Troilite (VCDT). The precision of sulfur isotopic analyses is better than ±0.2‰.

Eleven sulfides (pyrite, chalcopyrite, bornite, and enargite) and two fresh sandstones were selected for Fe isotope analyses. Iron dissolution and purification were carried out at the IGGCAS, following the established procedure (Zhao et al., 2015). Subsequently, the purified sample solutions were analyzed for Fe isotopes using a MC–ICP–MS (Thermo Neptune) at the University of Science and Technology of China (USTC), following previously published procedures (Huang et al., 2011). Instrumental mass fractionation was corrected using standard-sample bracketing. Iron isotope data are reported in standard δ notation in per mil (‰) relative to reference material IRMM-014, defined as $\delta^{x}Fe = [(\delta^{x}Fe/^{54}Fe)_{sample}/(\delta^{x}Fe/^{54}Fe)_{IRMM\text{-}014} - 1] * 1000$, where x is either 57 or 56. To assess the accuracy and long-term external precision of our analyses, At least two reference materials with Fe contents comparable to unknowns (BHVO-2 and BCR-2) were processed with unknown samples for each batch of column chemistry. The measured BHVO-2 and BCR-2 basalt standards yield $\delta^{57}Fe$ values of 0.15 ± 0.06‰ and 0.11 ± 0.07‰ (n = 6), consistent with their published values ($\delta^{57}Fe$ = 0.17 ± 0.02‰ and 0.12 ± 0.02‰; Craddock and Dauphas, 2011 and references therein) within uncertainty, suggesting that interlaboratory biases for Fe isotopes are negligible.

## 5. Results

### 5.1. Zircon U–Pb ages

Zircons from the studied samples were mostly euhedral, with elongated to short prismatic forms and lengths of 100–300 μm (Fig. 5). Most zircons show oscillatory zoning (Fig. 5) and Th/U ratios of 0.35–0.82, consistent with characteristic of igneous zircons (Corfu et al., 2003). The zircon U–Pb ages can be interpreted as representing the crystallization age of the host rocks.

Two argillic granodiorite porphyries ND-1 and NDZK001-81 (Fig. 5a, b) yielded $^{206}Pb/^{238}U$ weighted mean ages of 119.1 ± 1.3 Ma (n = 23; MSWD = 0.7) and 116.1 ± 1.3 Ma (n = 14; MSWD = 0.7), respectively.

**Table 1**
Representative EMPA results for sulfides from the Nadun Cu–Au mineralization, central Tibet

| Sample | Nd005-128 | | | | | Nd001-48 | | | Nd001-145 | |
|---|---|---|---|---|---|---|---|---|---|---|
| Description | Quartz–pyrite–chalcopyrite–enargite vein | | | | | Breccia | | | Breccia | |
| Minerals (wt.%) | Enargite | | Tennantite | | Pyrite | Bornite | Digenite | | Chalcopyrite | |
| As | 17.75 | 18.40 | 17.72 | 19.25 | 0.00 | 0.00 | 0.00 | 1.64 | 0.00 | 0.00 |
| Se | 0.00 | 0.00 | 0.03 | 0.00 | 0.00 | 0.03 | 0.01 | 0.02 | 0.00 | 0.00 |
| Ag | 0.07 | 0.02 | 0.04 | 0.06 | 0.00 | 0.07 | 0.07 | 0.06 | 0.00 | 0.01 |
| S | 32.46 | 33.27 | 28.57 | 28.14 | 54.51 | 24.72 | 21.87 | 22.83 | 35.28 | 34.76 |
| Fe | 0.01 | 0.02 | 4.08 | 2.30 | 44.57 | 11.21 | 1.34 | 2.69 | 29.70 | 30.21 |
| Cu | 49.52 | 47.14 | 46.91 | 50.10 | 0.00 | 62.42 | 75.77 | 71.49 | 34.29 | 34.70 |
| Bi | 0.16 | 0.12 | 0.00 | 0.08 | 0.38 | 0.37 | 0.19 | 0.39 | 0.19 | 0.12 |
| Pb | 0.00 | 0.04 | 0.89 | 0.00 | 0.06 | 0.00 | 0.05 | 0.00 | 0.03 | 0.00 |
| Cd | 0.04 | 0.02 | 0.13 | 0.08 | 0.02 | 0.00 | 0.00 | 0.00 | 0.00 | 0.09 |
| Zn | 0.09 | 0.19 | 1.01 | 0.58 | 0.07 | 0.19 | 0.18 | 0.70 | 0.05 | 0.07 |
| Sb | 0.00 | 0.02 | 0.04 | 0.04 | 0.00 | 0.00 | 0.04 | 0.00 | 0.03 | 0.00 |
| Te | 0.04 | 0.03 | 0.02 | 0.00 | 0.00 | 0.00 | 0.00 | 0.00 | 0.00 | 0.00 |
| Ni | 0.02 | 0.03 | 0.00 | 0.03 | 0.01 | 0.01 | 0.02 | 0.03 | 0.00 | 0.00 |
| Co | 0.00 | 0.00 | 0.01 | 0.02 | 0.05 | 0.00 | 0.00 | 0.02 | 0.04 | 0.06 |
| Mn | 0.01 | 0.00 | 0.02 | 0.01 | 0.00 | 0.01 | 0.00 | 0.00 | 0.01 | 0.00 |
| Sn | 0.01 | 0.00 | 0.00 | 0.02 | 0.00 | 0.00 | 0.00 | 0.00 | 0.01 | 0.00 |
| Total | 100.16 | 99.30 | 99.46 | 100.71 | 99.67 | 99.04 | 99.54 | 99.86 | 99.63 | 100.02 |
| As | 0.116 | 0.120 | 0.117 | 0.128 | 0.000 | 0.000 | 0.000 | 0.011 | 0.000 | 0.000 |
| Se | 0.000 | 0.000 | 0.000 | 0.000 | 0.000 | 0.000 | 0.000 | 0.000 | 0.000 | 0.000 |
| Ag | 0.000 | 0.000 | 0.000 | 0.000 | 0.000 | 0.000 | 0.000 | 0.000 | 0.000 | 0.000 |
| S | 0.495 | 0.509 | 0.442 | 0.437 | 0.677 | 0.393 | 0.358 | 0.371 | 0.506 | 0.490 |
| Fe | 0.000 | 0.000 | 0.036 | 0.021 | 0.318 | 0.102 | 0.013 | 0.025 | 0.245 | 0.245 |
| Cu | 0.381 | 0.364 | 0.366 | 0.393 | 0.000 | 0.501 | 0.626 | 0.586 | 0.248 | 0.247 |
| Bi | 0.000 | 0.000 | 0.000 | 0.000 | 0.001 | 0.001 | 0.000 | 0.001 | 0.000 | 0.000 |
| Pb | 0.000 | 0.000 | 0.002 | 0.000 | 0.000 | 0.000 | 0.000 | 0.000 | 0.000 | 0.000 |
| Cd | 0.007 | 0.004 | 0.027 | 0.016 | 0.003 | 0.000 | 0.000 | 0.000 | 0.000 | 0.017 |
| Zn | 0.001 | 0.001 | 0.008 | 0.004 | 0.000 | 0.002 | 0.001 | 0.006 | 0.000 | 0.001 |
| Sb | 0.000 | 0.000 | 0.000 | 0.000 | 0.000 | 0.000 | 0.000 | 0.000 | 0.000 | 0.000 |
| Te | 0.000 | 0.000 | 0.000 | 0.000 | 0.000 | 0.000 | 0.000 | 0.000 | 0.000 | 0.000 |
| Ni | 0.000 | 0.000 | 0.000 | 0.000 | 0.000 | 0.000 | 0.000 | 0.000 | 0.000 | 0.000 |
| Co | 0.000 | 0.000 | 0.000 | 0.000 | 0.000 | 0.000 | 0.000 | 0.000 | 0.000 | 0.000 |
| Mn | 0.000 | 0.000 | 0.000 | 0.000 | 0.000 | 0.000 | 0.000 | 0.000 | 0.000 | 0.000 |
| Sn | 0.000 | 0.000 | 0.000 | 0.000 | 0.000 | 0.000 | 0.000 | 0.000 | 0.000 | 0.000 |
| Total | 1.000 | 1.000 | 1.000 | 1.000 | 1.000 | 1.000 | 1.000 | 1.000 | 1.000 | 1.000 |

One fresh quartz diorite porphyry (ND-10; Fig. 5c) yielded the youngest $^{206}Pb/^{238}U$ weighted mean age of 113.1 ± 1.9 Ma (n = 14; MSWD = 0.1), and roughly shows three groups of inherited zircon ages: ~120 Ma, ~130Ma, and ~150 Ma.

### 5.2. Zircon Hf isotopes

Most zircons from the ~119 Ma argillic granodiorite porphyry ND-1 showed relatively restricted εHf(t) values ranging from 1.4 to 8.1 (mean = 5.2 ± 1.1; n = 18), except for two grains with εHf(t) values of −2.0 and −8.8 (Fig. 6). The ~113 Ma fresh quartz diorite porphyry ND-10 showed relatively consistent zircon εHf(t) values of 1.2–7.6 (mean = 4.8 ± 1.1; n = 14) similar to the ~119 Ma argillic granodiorite porphyry (Fig. 6). The three groups of inherited zircons have εHf(t) values of 5.0–5.7, 4.9–5.5, and 5.8, respectively.

### 5.3. Compositions of sulfides

The enargite contains 17.75–19.66 wt.% As, 32.46–33.27 wt.% S, 49.52–50.13 wt.% Cu, and minor Fe, Bi, and Zn (Table 1). The tennanite has lower S (28.14–28.57 wt.%) and higher Fe content (2.3–4.08 wt.%) while the pyrite contains 53.39–54.51 wt.% S and 43.87–45.27 wt.% Fe, and minor 0.20–0.38 wt.% Bi and 0–0.34 wt.% Cu. The bornite contains 62.42 wt.% Cu, 24.72 wt.% S, 11.21 wt.% Fe, 0.37 wt.% Bi and 0.19 wt.% Zn. The digenite contains 21.87–22.83 wt.% S, 71.49–75.77 wt.% Cu, and minor 0.19–0.39 wt.% Bi, 0.18–0.70 wt.% Zn, 0–1.64 wt.% As and 1.34–2.69 wt.% Fe. The chalcopyrite contains 34.65–35.61 wt.% S, 32.51–34.70 wt.% Cu, 29.70–30.36 wt.% Fe, and minor 0.09–0.20 wt.% Bi and 0–0.11 wt.% Zn.

### 5.4. Fluid inclusions

Based on phase proportions at room temperature, three types of fluid inclusions were identified: (1) vapor-rich inclusions; (2) liquid-rich inclusions; (3) brine inclusions with halite (and/or sylvite) daughter minerals (Fig. 8). All types of fluid inclusions were found in the pre-ore quartz–pyrite veins from the argillic alteration zone. Bellow breccia, the proportion of vapor-rich inclusions gradually decreases with increasing depth (Fig. 9) and likely formed a vapor-rich shell. In the quartz–pyrite veins, vapor-rich inclusions homogenize to the vapor phase between 323 and 490 °C (Fig. 10a) and have a salinity ranging from 1.1 to 11.3 wt.% NaCl equivalent (Fig. 10b), whereas brine inclusions have homogenization temperatures (by vapor or halite disappearance) from 227 to > 550 °C (Fig. 10a) and salinities of 27.4–41.2 wt.% NaCl equivalent (Fig. 10b; Table 2). Moreover, possible boiling assemblages (Fig. 8f) of vapor-rich inclusions coexisting with brine-rich ones occur on pseudosecondary trails. Generally, microthermometric results reveal the two type of inclusions show relatively consistent homogenization temperatures of ~300 to 500 °C (Figs. 8f, 10a, 11). Unfortunately, vapor-rich inclusions coexisting with brines (homogenization temperatures > 500 °C) in boiling assemblages were different to utilize for microthermometry owing to the low visibility of the liquid. Therefore, the homogenization temperatures for these boiling assemblages were inferred from coexisting brines. In addition, liqiud-rich inclusions were homogenized (given by vapor disappearance) at 232–393 °C

**Table 2**
Microthermometric data of fluid inclusions of the Nadun Cu–Au mineralization, central Tibet.

| Sample no. | Description | Proportion of fluid inclusions | Phases | Shape | Size (μm) | V/L (vol.%) | Tm (°C) | Tv (°C) | $T_{KCl}$ (°C) | $T_{NaCl}$ (°C) | Th (°C) | Salinity (wt.% NaCl equiv.) |
|---|---|---|---|---|---|---|---|---|---|---|---|---|
| *Ore body* | | | | | | | | | | | | |
| NDZK001-27 | Breccia | 100% L | L+V | Oval, negative crystal shape | 5–42 | 5–30 | −3.9 to −15.8 | 193–356 | | | 193–356 | 6.3–19.3 |
| NDZK001-44 | Breccia | 100% L | L+V | Oval, negative crystal shape | 6–21 | 15–35 | −3.2 to −1.0 | 198–342 | | | 198–342 | 1.7–5.3 |
| NDZK001-74 | Breccia | 100% L | L+V | Oval, negative crystal shape | 5–21 | 15–40 | −6.9 to −1.0 | 289–424 | | | 289–424 | 3.2–9.2 |
| NDZK005-120 | Q-Py-Cp-En vein | 100% L | L+V | Oval, negative crystal shape | 7–23 | 15–40 | −6.2 to −1.6 | 182–359 | | | 182–359 | 2.7–9.5 |
| *Not in ore body* | | | | | | | | | | | | |
| NDZK004-360 | Q-Py vein | 15% L | L+V | Oval, negative crystal shape | 7–28 | 15–30 | −4.6 to −0.5 | 325–386 | | | 325–386 | 0.9–7.3 |
| | | 80% V | L+V | | 7–18 | 85–90 | −1.2 to −0.6 | | | | 338–434 | 1.1–2.1 |
| | | 5% B | L+V+H | | 5–16 | 15–25 | | 259–407 | | 133–286 | 259–407 | 29.0–36.9 |
| NDZK005-394 | Q-Py vein | 40% L | L+V | Oval, negative crystal shape | 7–25 | 15–35 | −6.5 to −0.9 | 299–365 | | | 299–365 | 1.6–9.9 |
| | | 40% V | L+V±Op | | 8–21 | 80–95 | −3.5 to −0.7 | | | | 362–443 | 1.2–5.7 |
| | | 10% B | L+V+H±Op | | 5–13 | 15–30 | | | | 195–253 | 244–>550 | 31.6–34.9 |
| NDZK005-256 | Q-Py vein | 15% L | L+V | Oval, negative crystal shape | 7–19 | 20–40 | −12.2 to −1.0 | 232–350 | | | 232–350 | 1.7–16.1 |
| | | 80% V | L+V | | 5–25 | 80–90 | −7.7 to −1.1 | | | | 390–416 | 1.9–11.3 |
| | | 5% B | L+V+H | | 7–10 | 15–20 | | 268–439 | | 128–295 | 268–439 | 28.9–37.8 |
| NDZK005-408 | Q-Py vein | 67% L | L+V | Oval, negative crystal shape | 7–25 | 20–40 | −7.7 to −0.6 | 301–341 | | | 301–341 | 1.1–11.3 |
| | | 30% V | L+V | | 6–23 | 85–90 | −2.1 to −1.5 | | | | 315–409 | 2.6–3.5 |
| | | 3% B | L+V+H | | 7–13 | 15–25 | | | | 134–267 | 321–389 | 29.1–35.8 |
| NDZK004-220 | Q-Py vein | 13% L | L+V | Oval, negative crystal shape | 4–18 | 20–35 | −12.1 to −0.3 | 283–376 | | | 283–376 | 0.5–16.1 |
| | | 82% V | L+V | | 8–21 | 85–92 | −2.9 to −0.7 | | | | 323–379 | 1.2–4.8 |
| | | 5% B | L+V+H | | 8–14 | 20–30 | | | | 250–285 | 302–337 | 34.7–37.0 |
| NDZK004-175 | Q-Py vein | 7% L | L+V | Oval, negative crystal shape | 7–18 | 15–40 | −10.6 to 0.2 | 264–378 | | | 264–378 | 0.4–14.6 |
| | | 90% V | L+V | | 10–20 | 85–95 | −6.4 to 1.4 | | | | 323–410 | 3.6–9.7 |
| | | 3% B | L+V+H | | 4–14 | 15–40 | | | | 76–284 | 262–>550 | 27.4–37.0 |
| NDZK005-288 | Q-Py vein | 20% L | L+V | Oval, negative crystal shape | 8–16 | 15–25 | −7.2 to −1.5 | 298–354 | | | 298–354 | 2.6–10.7 |
| | | 70% V | L+V | | 7–14 | 85–90 | −3.2 to −4.9 | | | | 431–472 | 5.3–7.7 |
| | | 10% B | L+V+H | | 4–14 | 15–35 | | | 110–135 | 120–289 | 238–>550 | 28.6–37.3 |
| NDZK004-342 | Q-Py vein | 15% L | L+V | Oval, negative crystal shape | 8–45 | 15–30 | −10.6 to −0.4 | | | | 299–393 | 0.7–14.6 |
| | | 80% V | L+V | | 7–25 | 85–90 | −0.9 to −0.7 | | | | 388–410 | 1.2–1.6 |
| | | 5% B | L+V+H | | 5–15 | 15–25 | | | | 261–318 | 281–>550 | 35.4–41.2 |

Abbreviations: Py—pyrite, En—enargite, Cp—chalcopyrite, Q—quartz, V—vapor, L—liqiud, B—brine, Tm—temperature of ice-melting, Tv—temperature of vapor disappearance, $T_{KCl}$—temperature of sylvite metling, $T_{NaCl}$—temperature of halite metling, Th—homogenization temperature.

**Table 3**
Oxygen and hydrogen isotope data of quartz from the Nadun Cu–Au mineralization, central Tibet.

| Sample no. | Description | Mineral | $^{18}O_{quartz}$ (‰) | T (°C)[a] | $^{18}O_{fluid}$ (‰)[b] | $D_{fluid}$ (‰) |
|---|---|---|---|---|---|---|
| *Ore body* | | | | | | |
| NDZK001-27 | Breccia | Quartz | 11.1 | 315 | 4.8 | −102 |
| NDZK001-33 | Breccia | Quartz | 8.4 | 310 | 1.9 | −106 |
| NDZK001-50 | Breccia | Quartz | 6.6 | 320 | 0.4 | −88 |
| NDZK001-60 | Breccia | Quartz | 8.8 | 320 | 2.6 | −96 |
| NDZK001-74 | Breccia | Quartz | 7.9 | 340 | 2.3 | −107 |
| *Not in ore body* | | | | | | |
| NDZK004-175 | Quartz–pyrite vein | Quartz | 12.3 | 350 | 7.0 | −93 |
| NDZK004-218 | Quartz–pyrite vein | Quartz | 12.9 | 335 | 7.2 | −70 |
| NDZK004-220 | Quartz–pyrite vein | Quartz | 15.0 | 350 | 9.7 | −70 |
| NDZK004-296 | Quartz–pyrite vein | Quartz | 14.4 | 335 | 8.7 | −77 |
| NDZK004-342 | Quartz–pyrite vein | Quartz | 11.2 | 340 | 5.6 | −71 |
| NDZK005-256 | Quartz–pyrite vein | Quartz | 14.0 | 340 | 8.4 | −79 |
| NDZK005-394 | Quartz–pyrite vein | Quartz | 13.3 | 370 | 8.5 | −66 |
| NDZK005-424 | Quartz–pyrite vein | Quartz | 11.6 | 380 | 7.1 | −73 |

[a] Temperatures (T) are obtained from the fluid inclusion homogenization temperatures.
[b] Calculated $\delta^{18}O_{fluid}$ values are determined using isotope fractionation equation of $10\ln\alpha_{quartz-H2O} = 3.34 \times 10^6 T^{-2} - 3.31$ (Matsuhisa et al., 1979).

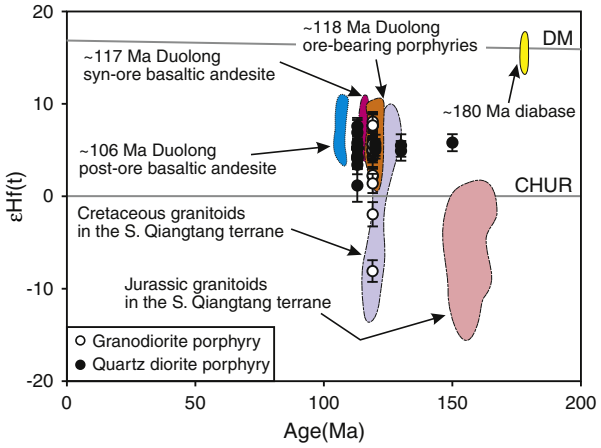


**Fig. 7.** Zircon εHf(t) values versus Age (Ma) diagram of granodiorite porphyry and quartz diorite porphyry from the Nadun Cu–Au mineralization. Data for syn- and post-ore basaltic andesite and ore-bearing granodiorite porphyries of Duolong porphyry Cu–Au deposit are from Chen et al. (2013), Li et al. (2013, 2016), Zhu et al. (2015a). Data for Cretaceous and Jurassic granitoids in the southern Qiangtang terrane are from Li et al. (2014). Data for Jurassic (~180 Ma) mantle-derived diabase in the southern Qiangtang terrane are from Li et al. (2015a).

and salinities of 0.4–16.1 wt.% NaCl equivalent (Fig. 10a, b). In contrast, only liqiud-rich inclusions were found in the breccia ore body (Fig. 9) with homogenization temperatures (given by vapor disappearance) of 193–424 °C and salinities of 1.7–19.3 wt.% NaCl equiv. (Figs. 10c, d, 11).

### 5.5. O and H isotopes

$\delta^{18}O$ values (n = 8) of quartz and δD values of fluid inclusion water from pre-ore quartz–pyrite vein in argillic alteration zone have a range from 11.6 to 15.0‰ and −66.0 to −93.1‰ (Table 3; Fig. 12), respectively. Based on the homogenization temperature of fluid inclusions, the estimated $\delta^{18}O$ values of fluids range between 7.08 and 9.71‰. Quartz from the breccia ore body shows $\delta^{18}O$ values (n = 5) between 6.6 and 11.1‰ and δD values of fluid inclusion water ranging from −88.1 to −102‰. The estimated $\delta^{18}O$ values of ore-forming fluids range from 0.42 to 4.75‰ (Table 3; Fig. 12).

**Table 4**
Iron and sulfur isotopic compositions of sulfides and sandstones from the Nadun Cu–Au mineralization, central Tibet.

| Sample no. | Description | Mineral | $\delta^{34}S$-Sulfide (‰) | $\delta^{34}S$–$H_2S$ (‰)[a] | $\delta^{57}Fe$ (‰) | 2SD | $\delta^{56}Fe$ (‰) | 2SD |
|---|---|---|---|---|---|---|---|---|
| *Ore body* | | | | | | | | |
| NDZK001-27 | Breccia | Chalcopyrite | −4.1 | −3.9 | | | | |
| NDZK001-33 | Breccia | Pyrite | −0.5 | −1.7 | | | | |
| NDZK001-33 | Breccia | Chalcopyrite | −5.9 | −5.7 | | | | |
| NDZK001-48 | Breccia | Pyrite | −0.5 | −1.7 | −0.48 | 0.08 | −0.32 | 0.04 |
| NDZK001-48 | Breccia | Chalcopyrite | −4.3 | −4.1 | −1.00 | 0.09 | −0.68 | 0.04 |
| NDZK001-48 | Breccia | Bornite | −2.4 | −1.6 | −0.82 | 0.06 | −0.53 | 0.04 |
| NDZK001-50 | Breccia | Pyrite | −1.0 | −2.2 | | | | |
| NDZK001-50 | Breccia | Chalcopyrite | −1.2 | −1.0 | | | | |
| NDZK001-60 | Breccia | Pyrite | −0.5 | −1.7 | | | | |
| NDZK001-60 | Breccia | Chalcopyrite | −1.7 | −1.5 | | | | |
| NDZK001-70 | Breccia | Pyrite | −1.6 | −2.8 | | | | |
| NDZK001-70 | Breccia | Chalcopyrite | −2.7 | −2.5 | | | | |
| NDZK001-145 | Breccia | Pyrite | −1.4 | −2.6 | −0.11 | 0.03 | −0.07 | 0.02 |
| NDZK001-145 | Breccia | Chalcopyrite | −3.3 | −3.1 | −0.97 | 0.09 | −0.65 | 0.03 |
| NDZK001-145 | Breccia | Enargite | −1.7 | | −1.11 | 0.07 | −0.74 | 0.03 |
| NDZK005-104 | Quartz–pyrite–enargite vein | Pyrite | 1.5 | 0.3 | −0.69 | 0.03 | −0.47 | 0.04 |
| NDZK005-104 | Quartz–pyrite–enargite vein | Enargite | 2.0 | | −2.15 | 0.09 | −1.44 | 0.03 |
| NDZK005-128 | Quartz–pyrite–enargite vein | Enargite | 1.0 | | | | | |
| *Not in ore body* | | | | | | | | |
| NDZK005-192 | Quartz–pyrite vein | Pyrite | −1.3 | −2.3 | | | | |
| NDZK005-394 | Quartz–pyrite vein | Pyrite | −0.9 | −1.9 | −0.25 | 0.01 | −0.17 | 0.01 |
| NDZK004-158 | Quartz–pyrite vein | Pyrite | −1.4 | −2.4 | | | | |
| NDZK004-175 | Quartz–pyrite vein | Pyrite | −0.9 | −1.9 | 0.10 | 0.02 | 0.07 | 0.02 |
| NDZK004-220 | Quartz–pyrite vein | Pyrite | −0.7 | −1.7 | | | | |
| NDZK004-238 | Quartz–pyrite vein | Pyrite | −1.1 | −2.1 | | | | |
| NDZK004-280 | Quartz–pyrite vein | Pyrite | 0.5 | −0.5 | | | | |
| NDZK004-374 | Quartz–pyrite vein | Pyrite | 3.7 | 2.7 | | | | |
| NDZK004-434 | Quartz–pyrite vein | Pyrite | −0.7 | −1.7 | 0.17 | 0.03 | 0.11 | 0.04 |
| DD-23 | Sandstone | Whole rock | | | 0.22 | 0.05 | 0.14 | 0.03 |
| DM-2 | Sandstone | Whole rock | | | 0.43 | 0.04 | 0.29 | 0.04 |
| BCR-2 | Basalt standard | Whole rock | | | 0.11 | 0.07 | 0.07 | 0.04 |
| BHVO-2 | Basalt standard | Whole rock | | | 0.12 | 0.06 | 0.08 | 0.05 |

[a] $\delta^{34}S$ values of $H_2S_{aq}$ in equilibrium with the sulfide minerals, calculated from the equations of Ohmoto and Rye (1979).

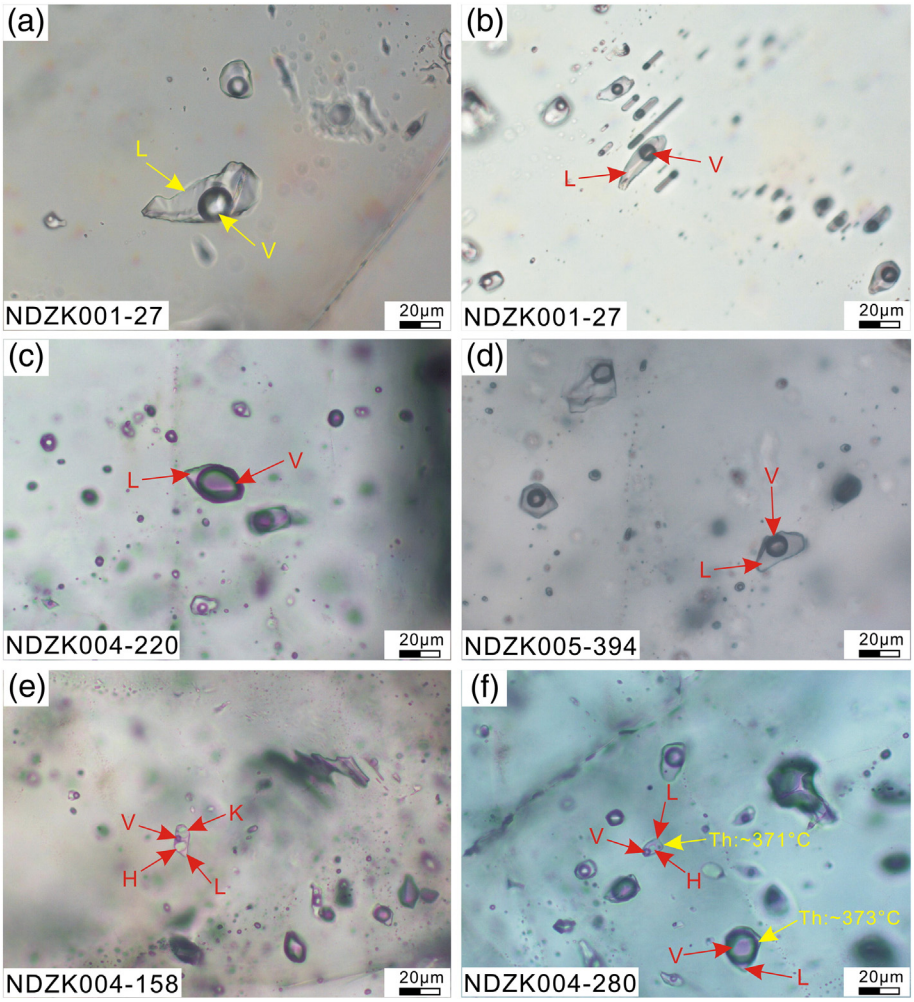


**Fig. 8.** Photographs of fluid inclusions from the Nadun Cu–Au mineralization. (a, b) Liquid-rich fluid inclusions (L) from breccia ore, and (c–f) vapor-rich (V), brine (B), and liquid-rich fluid inclusions from quartz–pyrite veins with sericite halo. Vapor-rich inclusion coexisting brine in figure f show relatively consistent homogenization temperatures (Th), likely suggesting a boiling assemblage.

### 5.6. S and Fe isotopes

The $\delta^{34}S$ values of sulfides (n = 27) from the Nadun mineralization have a wide range from −5.9 to 3.7‰ (Table 4; Fig. 13). Pyrite (n = 9) from the quartz–pyrite vein has $\delta^{34}S$ values between −1.4 and 3.7‰. The sulfides from the main breccia ore body show the lowest $\delta^{34}S$ values (<0‰), i.e., −1.6 to −0.5‰ in pyrite, −1.2 to −5.9‰ in chalcopyrite, −1.7‰ in enargite, and −2.4‰ in bornite. Enargite (n = 2) and pyrite (n = 1) from the quartz–enargite–pyrite veins in ore body (Fig. 3d) show high $\delta^{34}S$ values of 1–2‰ and 1.5‰, respectively.

The $\delta^{57}Fe$ values of sulfides also show a wide range between −2.15 and 0.17‰ (Table 4; Fig. 14). Pyrite (n = 3) from the quartz–pyrite vein yielded $\delta^{57}Fe$ values from −0.25 to 0.17‰. Enargite (n = 1) and pyrite (n = 1) from the quartz–enargite–pyrite vein show $\delta^{57}Fe$ values of −2.15‰ and −0.69‰, respectively. Pyrite from the breccia ore body has higher $\delta^{57}Fe$ values (−0.48 to −0.11‰) than chalcopyrite (−1.0 to −0.97‰), bornite (−0.82‰), and enargite (−1.11‰). Two fresh sandstone samples have $\delta^{57}Fe$ values of 0.22‰ and 0.43‰, respectively.

## 6. Disscusion

### 6.1. Ore deposit type of Nadun mineralization

High and intermediate sulfidation epithermal deposits are commonly spatially and temporally associated with underlying and adjacent porphyry systems (Hedenquist et al., 1998; Muntean and Einaudi, 2001). Based on the characteristics and classification of epithermal deposits (Hedenquist et al., 2000; Einaudi et al., 2003), high sulfidation epithermal deposits show a typical sulfide assemblage of enargite, tennantite, chalcopyrite and minor sphalerite and galena. Intermediate sulfidation deposits share many of the sulfide assemblages (but more sphalerite and galena) common to high sulfidation epithermal deposits, but the enargite-bearing assemblage is lacking. At Nadun, the main sulfide assemblage is enargite, tennantite, and minor galena. Combined with occurrence of locally advanced argillic alteration, this deposit may be classified as a high sulfidation epithermal deposit. Moreover, the roots of high sulfidation epithermal deposits can be narrow, with unmineralized quartz–pyrite veins and narrow to broad halos of sericitic alteration (Hedenquist et al., 2000). These quartz–pyrite veins were regarded as the channelways facilitating movement of ore-forming fluids from the porphyry to the epithermal system (Pudack et al., 2009). Thus, the zone of quartz–pyrite veins below the breccia ore in Nadun may represent the lower part of a typical high sulfidation epithermal deposit, similar to the Maricunga belt (Muntean and Einaudi, 2001). Additionally, the newly discovered Rongna porphyry-high sulfidation deposit (~1000 Mt ore resources at 0.6% Cu) is located ca. 15km north-east of the Nadun deposit (Li et al., 2015b), suggesting that the Duolong ore district is a porphyry-high sulfidation epithermal system. Based on these geological features, the quartz–pyrite veining with argillic alteration likely represents the upper part of a porphyry

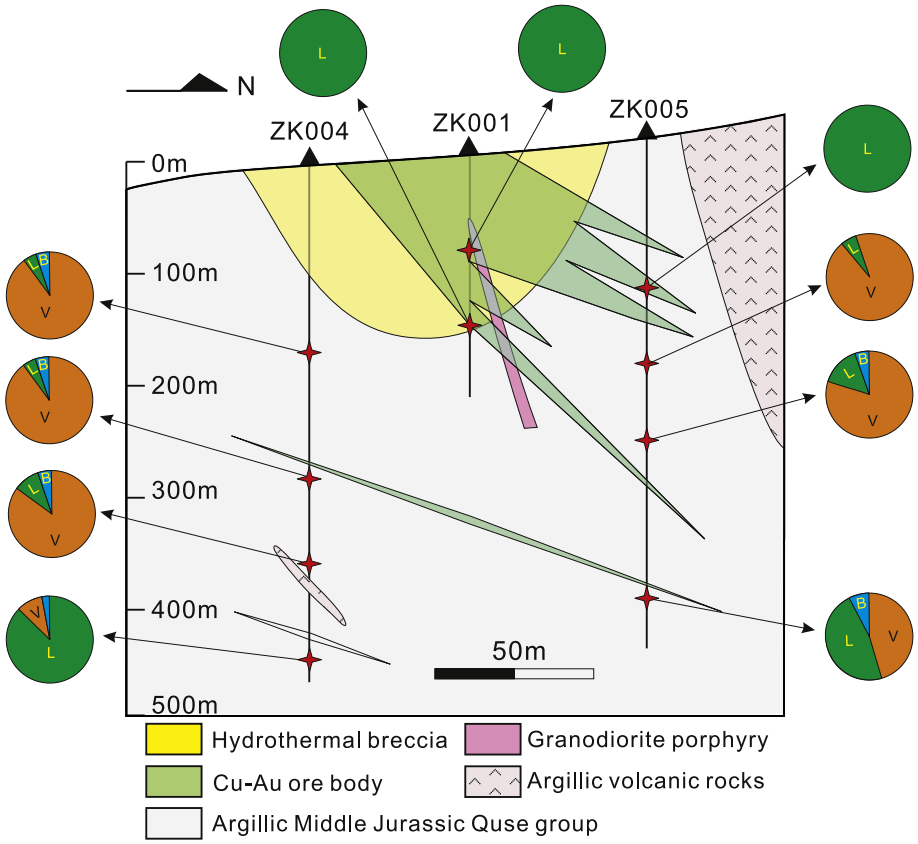


**Fig. 9.** Relative proportions of vapor-rich (V), liquid-rich inclusions (L), and brines (B) distributed in individual samples, and their spatial distribution in Nadun Cu–Au mineralization.

system, which then transitioned during later stages to shallow advanced argillic alteration with high sulfidation Cu–Au mineralization. Unfortunately, recent drilling has not discovered ore-forming porphyry below Nadun. The Nadun mineralization was either related to a deeper ore-forming porphyry or the Duolong porphyry, which will be confirmed by further exploration.

### 6.2. Timing of the Nadun Cu–Au mineralization

High sulfidation epithermal Cu–Au mineralization often has a close spatial and temporal relationship with adjacent porphyry Cu–Au deposits (e.g., Hedenquist and Lowenstern, 1994; Arribas et al., 1995; Hedenquist et al., 1998; Sillitoe, 2010; Richards, 2011). Previous geochronology studies (Fig. 15) indicated zircon U–Pb ages of ~117–119 Ma for ore-forming porphyries (Li et al., 2011b, 2013; Zhu et al., 2015a, b), molybdenite Re-Os ages of ~118–119 Ma (She et al., 2009; Zhu et al., 2015b), and ~115–119 Ma Ar-Ar ages for hydrothermal biotite, sericite, and K-feldspar (Li et al., 2011b; Zhu et al., 2012, 2015b) from the Duolong porphyry Cu–Au deposit. These ages constrained the duration of the magmatic–hydrothermal system at Duolong as between < 1 m.y. and ~6 m.y. (Fig. 15). At the adjacent Nadun mineralization, one strongly altered granodiorite porphyry (Fig. 5a) yielded a $^{206}Pb/^{238}U$ weighted mean age of 119.1 ± 1.3 Ma, consistent with the timing of ore formation at Duolong (~117–119 Ma) and the age of Duolong barren porphyries (~118–120 Ma; Li et al., 2011b, 2013). Recent exploration indicates that this granodiorite porphyry is not closely related to the breccia ore (Fig. 1d) and therefore, it may be an early intrusion, altered by late stage ore-forming fluids. Moreover, another granodiorite porphyry intruded into the tectonic–hydrothermal breccia and yielded a $^{206}Pb/^{238}U$ weighted mean age of 116.6 ± 1.3 Ma, indicating that the Nadun breccia mineralization likely occurred between ~116 and ~119 Ma, consistent with the duration of the Duolong magmatic–hydrothermal system (Fig. 15). The ~116 Ma granodiorite porphyry shows weak argillic alteration, likely due to the effect of fluid circulation, associated with emplacement. The fresh quartz diorite porphyry (Fig. 5c) yields the youngest $^{206}Pb/^{238}U$ weighted mean age of 113.1 ± 1.9 Ma, suggesting it is a post-ore intrusion. The relatively consistent ages between the Nadun and Duolong deposits indicates that they formed contemporaneously and resulted from the same magmatic–hydrothermal event (Fig. 15).

### 6.3. Petrogenesis of Nadun porphyries

Most studies indicate that Nadun and Duolong intermediate-felsic porphyries and syn/post-ore mafic–felsic volcanic rocks show high-K calc-alkaline compositions, with enrichment of light rare earth elements (LREE) and large ion lithophile elements (LILE: Cs and Rb) and depletion of high field strength elements (HFSE: Nb and Ti), consistent with the geochemical characteristics of arc-type magmas (Fu et al., 2014; Li et al., 2013, 2016). The Nadun porphyries have similar zircon U–Pb ages (Fig. 15) and Hf isotopic compositions (εHf(t) = 1.2–8.1; Fig. 7) as adjacent Duolong porphyries (εHf(t)=3.6–7.3; Li et al., 2013, 2016; Zhu et al., 2015a), likely indicating that they are comagmatic. Moreover, the Cretaceous Nadun porphyries have obviously higher zircon εHf(t) values (Fig. 7) than Jurassic–Cretaceous arc-type granitoids (Li et al., 2014) and lower values than mantle-derived diabase (εHf(t) = 14.8–16.1; Li et al., 2015a) in the southern Qiangtang terrane, suggesting mixing between mantle-derived and crust-derived melts. The presence of inherited zircon and wide ranging zircon εHf(t) values (−8.8 to 8.1; Fig. 7) in Nadun porphyries likely indicates an open magmatic system (Griffin et al., 2002; Li et al., 2014). The Nadun porphyries also show enriched Sr-Nd isotopic compositions

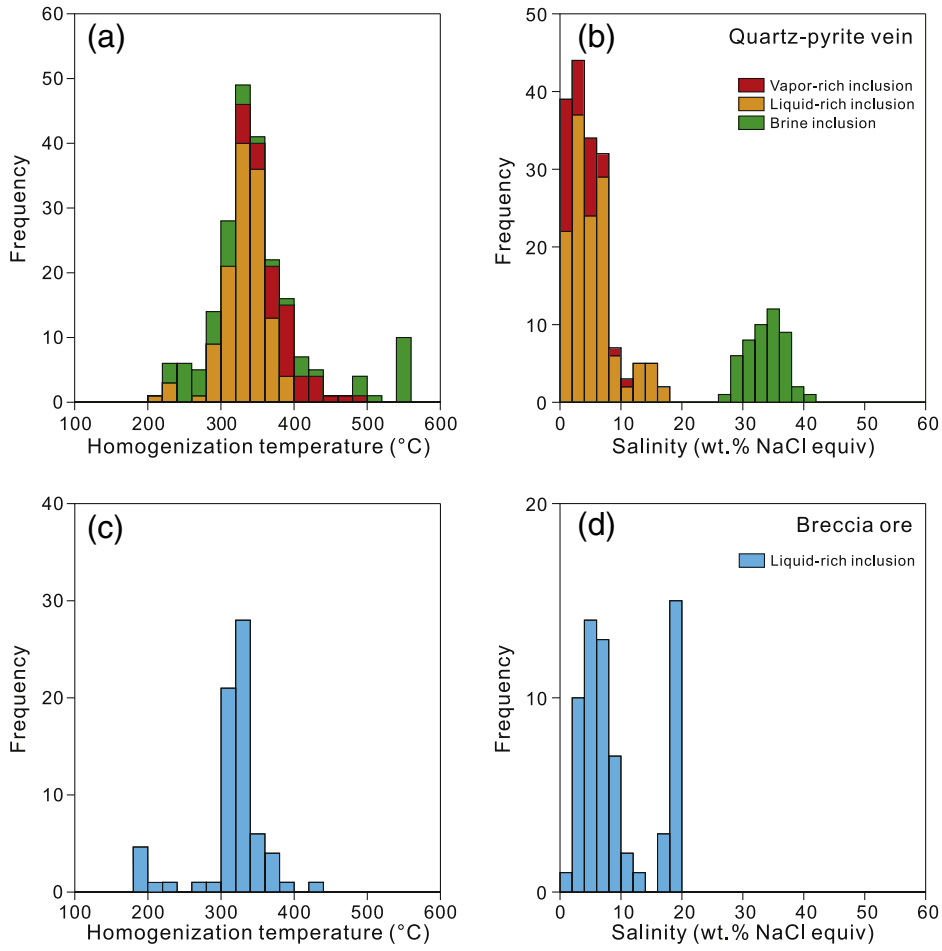


**Fig. 10.** Homogenization temperature and salinity histograms of fluid inclusions hosted in quartz from quartz–pyrite veins (a, b) and breccia ore (c, d).

($^{87}Sr/^{86}Sr_i$ values of 0.7085–0.7109, εNd(t) values ranging from −3.8 to −4.2; Fu et al., 2014) relative to syn/post-ore volcanic rocks in this ore district (initial Sr ratios of 0.7045–0.7055 and εNd(t) values of −0.8 to 3.6; Li et al., 2016), probably indicating a higher contribution from the Qiangtang crust. The data is consistent with the Nadun porphyries being derived by melting of metasomatized mantle wedge to form basaltic melts, that subsequently underwent MASH process (melting, assimilation, storage and homogenization; Hildreth and Moorbath, 1988) at the base of lower crust during northward subduction of Bangong–Nujiang oceanic plate (Li et al., 2013, 2016).

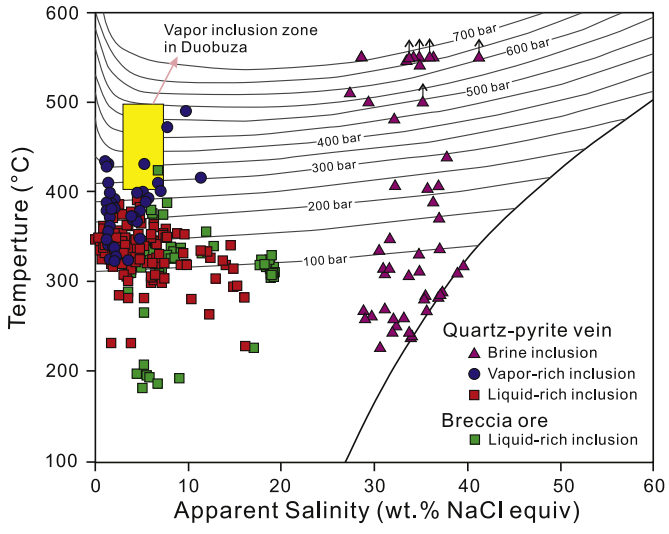


**Fig. 11.** Summary plot of homogenization temperatures and salinities of fluid inclusions for the Nadun Cu–Au mineralization, central Tibet. Vapor–liquid coexistence curves were calculated from the equations of Driesner and Heinrich (2007). Data of vapor-rich fluid inclusions are from Li et al. (2007).

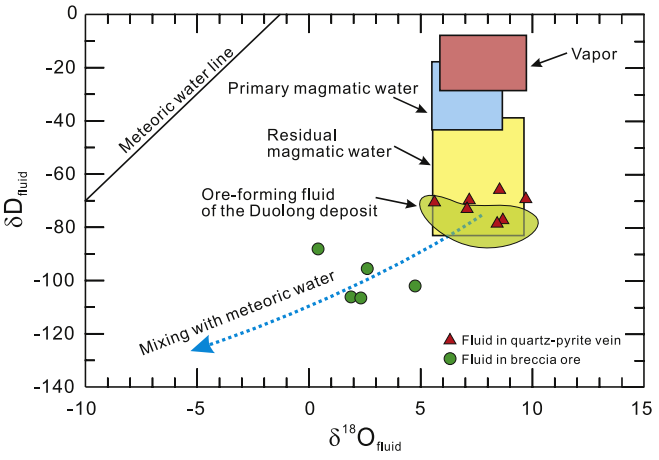


**Fig. 12.** O and H isotopic compositions of ore-forming fluids from the Nadun Cu–Au mineralization, central Tibet. Data of the Duolong porphyry Cu–Au deposit from Li (2008).

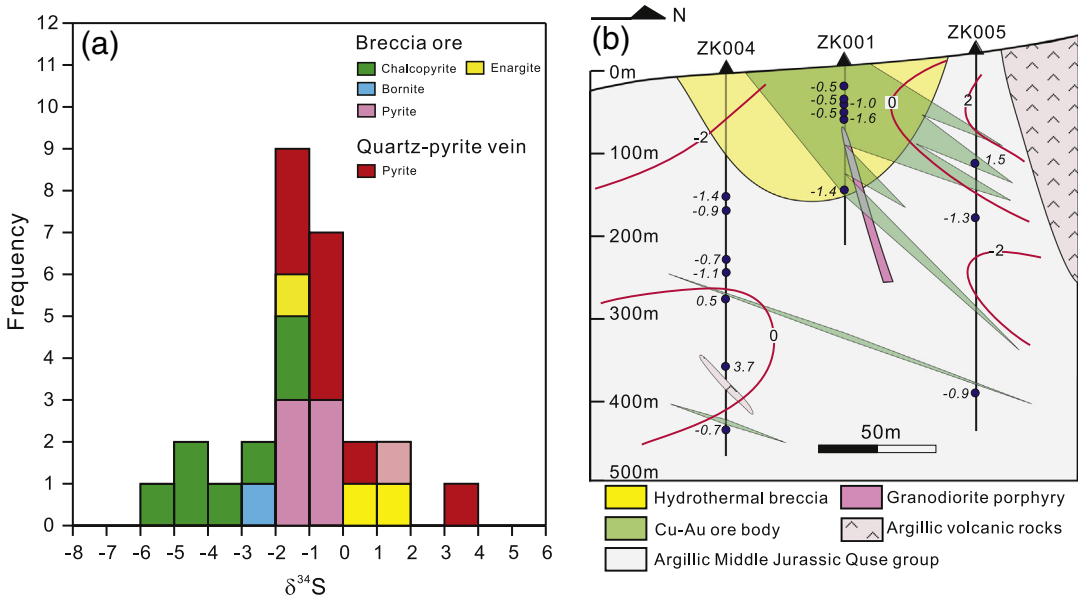


**Fig. 13.** (a) Histogram of S isotope compositions of sulfides and (b) spatial distribution of $\delta^{34}S$ values of pyrites from the Nadun Cu–Au mineralization, central Tibet.

### 6.4. Evolution and sources of ore-forming fluid

In the quartz–pyrite veins, boiling assemblages in vapor-rich inclusions coexisting with brines likely record successive phase separation with decreasing temperature (>550 to 300 °C) and pressure (>700–110 bar; Fig. 11). Liquid-rich fluid inclusions from quartz–pyrite veins, especially at deeper levels of the Nadun mineralization (Fig. 9), likely represent the waning stage of a porphyry system, similar to quartz–sericite–pyrite veins from the Nevados de Famatina porphyry–epithermal system, Argentina (Pudack et al., 2009). O and H isotopic compositions of the ore-forming fluids that formed quartz–pyrite veins ($\delta^{18}O_{fluid}$ = 7.08–9.71‰ and δD = −93.1 to −66‰) plot in the field of residual magmatic water, indicating a magmatic source (Fig. 12). During the breccia stage, only liquid-rich inclusions occur and these yield homogenization temperatures of 193–424 °C and salinities of 1.7–19.3 wt.% NaCl equivalent (Fig. 10c, d). Most liquid-rich inclusions show a similar salinity as vapor-rich inclusions from quartz–pyrite veins (salinity ranging from 1.1 to 11.3 wt.% NaCl equivalent; Fig. 11), likely indicating these inclusions were caused by vapor contraction during cooling at elevated presssure, above the critical curve of the salt-water system (Heinrich et al., 2004; Heinrich, 2005; Pudack et al., 2009). Previous studies suggested that vapor-rich inclusions may be derived from early stage boiling or magma exsolution at depth, representing fluids that transport Au and Cu to epithermal hydrothermal systems (Heinrich et al., 2004). Therefore, quartz–pyrite veins may be the channelways for metal-rich fluids from porphyry to epithermal system, as described by Pudack et al. (2009). Additionally, some inclusions show increasing salinity with decreasing temperature, possibly indicating mixing between liuquid-rich fluids and cooling brines during convective circulation (Fig. 11). Rare liquid-rich fluid inclusions show the lowest homogenization temperature (lower than 200 °C), likely indicating fluid cooling and/or dilution by meteoric water. The O and H isotopic values of ore-forming fluids ($\delta^{18}O_{fluid}$ = 0.42–4.75‰ and δD = −102 to −88.1‰) at the breccia stage indicate a minor addition of meteoric water (Fig. 12), similar to that proposed for fluids at the Pueblo Viejo epithetrmal Au-Ag deposit, Dominican Republic (Vennemann et al., 1993).

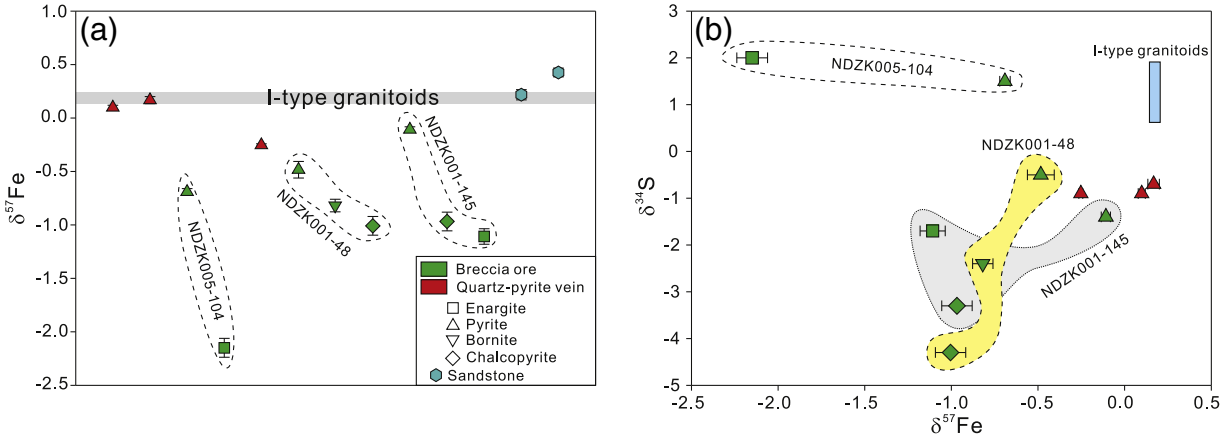


**Fig. 14.** Fe isotope ratios of sulfides and sandstones (a), and $\delta^{57}Fe$ versus $\delta^{34}S$ values of sulfides (b) from the Nadun mineralization, central Tibet. Fe and S isotopic data of I-type granitoids are from Foden et al. (2015) and Rye (1993), respectively.

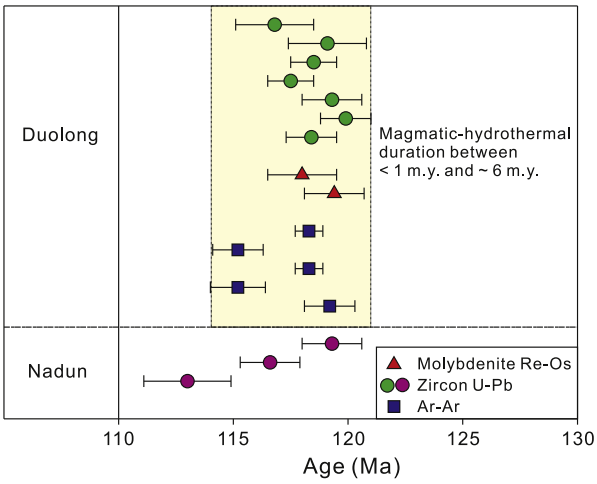


**Fig. 15.** Age spectrum of Duolong porphyry deposit and Nadun mineralization. Zircon U–Pb ages data for Duolong ore-bearing porphyries are from Li et al. (2011b, 2013) and Zhu et al. (2015a, b). Molybdenite Re–Os ages data from She et al. (2009) and Zhu et al. (2015b). Ar–Ar ages data for hydrothermal K-feldspar, sericite, and biotite are from Li et al. (2011b) and Zhu et al. (2012, 2015b).

A $\delta_{sulfate}$–$\delta_{sulfide}$ diagram can be used to estimate the oxidation state, bulk sulfur composition, and $H_2S/SO_4^{2-}$ ratio of the ore-forming fluids (Rye, 1993, 2005; Bethke et al., 2005; Seal, 2006). Based on homogenization temperature of fluid inclusions, the $\delta^{34}S$ values of $H_2S_{aq}$ in equilibrium with the sulfide minerals (Table 4), can be calculated from the equations of Ohmoto and Rye (1979). $\delta^{34}S$ values of fluids in equilibrium with pyrites from the breccia ore and quartz–pyrite veins show relatively consistent S isotopic ratios ($\delta^{34}S$ values ranging from −1.7 to −2.8; Fig. 16). Combined with S isotopic compositions of pyrite/chalcopyrite–gypsum pairs from Duolong deposit (Li, 2008; Xiao, 2012), ore-forming fluids in this stage likely were dominated by $H_2S$ and were relatively reduced (Fig. 16). Petrography observations show that chalcopyrite, bornite, and enargite occur as fillings into fractures

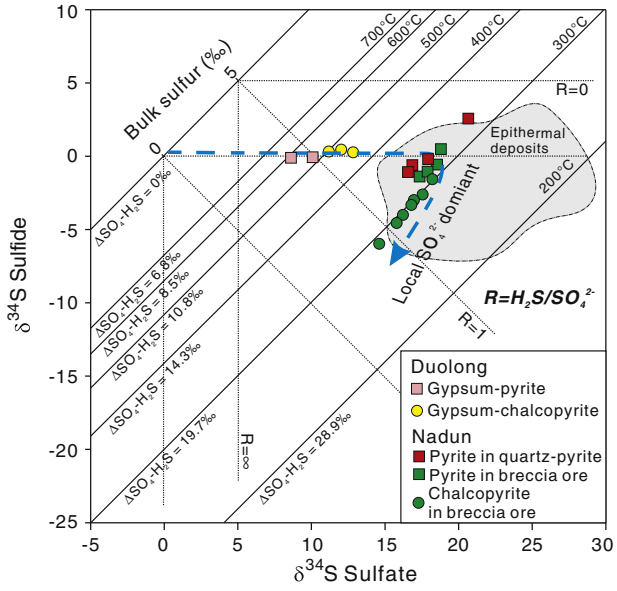


**Fig. 16.** $\delta_{sulfate}$–$\delta_{sulfide}$ diagram of the Nadun mineralization (Bethke et al., 2005). Although isotopic values of sulfates are not shown, the plots can be drawn based on $\delta^{34}S$ values of sulfides and temperatures estimated by fluid inclusions, assuming that isotope equilibrium between $H_2S$ and $SO_4^{2-}$ aqueous species in the fluids. S isotopic data of high sulfidation epithermal deposits from Seal (2006). S isotopic compositions of gypsum–chalcopyrite and –pyrite pairs are from Li (2008) and Xiao (2012), respectively.

in pyrite in breccia ore (Figs. 3d, 5a, c), suggesting the Cu-bearing minerals formed later. At this stage, bulk sulfur compositions of the ore-forming fluids show a downward shift (Fig. 16), likely suggesting that ore-forming fluids gradually become $SO_4^2$-rich (elevated $H_2S/SO_4^{2-}$ ratios) and relatively oxidized (Rye, 2005; Bethke et al., 2005). Therefore, the evolution of S isotope compositions could be attributed to $SO_2$ disproportionation and pyrite deposition, which lead to increased $\delta^{34}S$ and $SO_4^{2-}/H_2S$ ratios ($SO_4^2$-predominant) in ore-forming fluids (Fig. 16; Bethke et al., 2005; Cooke et al., 2011). However, pyrites from quartz–sulfides veins, and enargites and pyrites from breccia ore show high and positive $\delta^{34}S$ values of 1.0–3.7‰ (Fig. 13). Previous studies indicate that enargite-bearing assemblages should form in relatively oxidized fluids (Einaudi et al., 2003). Therefore, the heavy S isotopic compositions of these sulfides cannot be explained by $H_2S$-rich fluids that were relatively reduced. We speculatively suggest that these heavy S isotopic compositions may be a result of ore-forming fluids with high $\delta^{34}S$ values, which likely inherited this character during sulfur extraction from nearby arc-type basaltic andesites (Fig. 9) with high $\delta^{34}S$ values, similar with high oxidized arc magmas of high $\delta^{34}S$ values (~8‰; Imai et al., 1993).

Recently, Fe isotopes have proven to be an effective tool for assessing the evolution of ore-forming fluids and mineral precipitation in many deposits (e.g., Wawryk and Foden, 2015; Graham et al., 2004; Wang et al., 2015). At Nadun, pyrite from quartz–pyrite veins in the argillic alteration zone show higher $\delta^{57}Fe$ values ($\delta^{57}Fe = -0.25$ to 0.17‰) than those from breccia ore ($\delta^{57}Fe = -0.69$ to −0.11‰; Fig. 14). These pyrites formed in relatively homogeneous $H_2S$-rich magmatic fluids, suggested by consistent S isotopic compositions (Figs. 13b, 16). Combined with high $\delta^{57}Fe$ values (0.22–0.43‰) for the sandstone wall rock, the large variations of Fe isotopic compositions could result from rayleigh fractionation processes (pyrite precipitation), because pyrites have heavier Fe isotopic ratios than fluids they are in equilibrium with (Polyakov and Soultanov, 2011; Syverson et al., 2013). Obviously, Cu-bearing sulfides (chalcopyrite, bornite, and enargite) show lighter Fe isotopic compositions ($\delta^{57}Fe = -2.15$ to −0.82‰; Fig. 16). H and O isotopic compositions indicate that small amounts of meteoric water were added into ore-forming fluids during breccia formation (Fig. 12). Combined with ~0.1‰ $\delta^{57}Fe$ ratios for meteoric water (Beard and Johnson, 2004) and ~0.22–0.43‰ for sandstone (Fig. 14a), minor meteoric water interaction with wall rock can be ruled out when interpreting the Fe isotope variations of Cu-bearing sulfides. Precipitation of high $\delta^{57}Fe$ ratios minerals is proposed to explain Fe isotope variations. During breccia formation, $SO_2$ disproportionation meant that the ore-forming fluids gradually became $SO_4^2$-rich and highly oxidized, as indicated by the evolution of S isotopic compositions (Fig. 16). Under this hydrothermal environment, $Fe^{3+}$-bearing hematite and rutile with high $\delta^{57}Fe$ ratios precipitated, leading to light Fe isotopic compositions in the residual ore-forming fluids (Schauble, 2004; Polyakov and Soultanov, 2011; Syverson et al., 2013). In addition, $Fe^{3+}$-bearing bornite has higher $\delta^{57}Fe$ ratios (−0.82‰) than $Fe^{2+}$-bearing chalcopyrite (−1.00‰) in breccia sample NDZK001-48 (Fig. 14), likely due to $Fe^{3+}$-bearing minerals preferentially incorporating heavy Fe isotopes (Schauble, 2004).

## 7. Conclusions

(1) The Nadun high sulfidation epithermal Cu–Au occurrence is adjacent to the Cretaceous giant Duolong porphyry Cu–Au deposit within the Bangong–Nujiang metallogenic belt, central Tibet. Zircon U–Pb ages of two argillic granodiorite porphyries and one fresh quartz diorite porphyry show that Nadun mineralization formed between ~116 and ~119 Ma, consistent with the duration of the magmatic–hydrothermal system at Duolong. The Duolong and Nadun porphyries also have similar zircon εHf(t) values ranging from −8.8 to 8.1 (mean = 5.0 ± 1.1). These results indicate that they formed contemporaneously during the same magmatic–hydrothermal event.

(2) Vapor-rich inclusions in quartz–pyrite veins have similar salinity to liquid-rich inclusions in breccia ore, suggesting that vapor likely transported Cu and Au from the porphyry to the epithermal hydrothermal system, with subsequent vapor contraction occurring during cooling at elevated presssure. O and H isotopic compositions reveal that ore-forming fluids are dominantly derived from a magmatic source with only minor addition of meteoric water at a later stage.

(3) S isotope compositions of sulfides indicate ore-forming fluids gradually became $SO_4^2$-rich and relatively oxidized relative to their original $H_2S$-rich and reduced state. Pyrites from quartz–pyrite veins show higher $\delta^{57}Fe$ values than pyrites and Cu-bearing sulfides from breccia ore, likely suggesting precipitation and fractionation of $Fe^{3+}$-bearing hematite, rutile, and pyrite with heavier Fe isotopic compositions.

## Acknowledgments

This article was funded by the Natural Science Foundation Project (Grant No. 40902027), the Ministry of Science and Technology of China (973Project 2011CB403106), the "Strategic Priority Research Program" of the Chinese Academy of Sciences (Grant No. XDB03010303). We obtained support and help from senior geologists Hong-Qi Chen and Yu-Bin Li at the No.5 Geological Team, Tibet Bureau of Geology and Exploration. We also obtained specific guidance and assistance from Yue-Heng Yang concerning the analyses of LA-ICP-MS zircon geochronology and in-situ Hf isotopes, and Xin-Miao Zhao and Hui-Hui Cao concerning the analyses of Fe isotopes at the Institute of Geology and Geophysics, Chinese Academy of Sciences. This manuscript benefited from constructive comments by the editor Franco Pirajno and Hua-Yong Chen, and two anonymous reviewers and Dr. Zhi-Ming Yang.

## Appendix A. Supplementary data

Supplementary data to this article can be found online at http://dx.doi.org/10.1016/j.oregeorev.2016.04.019.

## References

Andersen, T., 2002. Correction of common lead in U–Pb analyses that do not report $^{204}Pb$. Chem. Geol. 192, 59–79.
Arribas, A., Hedenquist, J.W., Itaya, T., Okada, T., Concepcion, R.A., Garcia, J.S., 1995. Contemporaneous formation of adjacent porphyry and epithermal Cu–Au deposits over 300 ka in northern Luzon, Philippines. Geology 23, 337–340.
Beard, B.L., Johnson, C.M., 2004. Fe isotope variations in the modern and ancient earth and other planetary bodies. Rev. Mineral. Geochem. 55, 319–357.
Bethke, P.M., Rye, R.O., Stoffregen, R.E., Vikre, P.G., 2005. Evolution of the magmatic–hydrothermal acid-sulfate system at Summitville, Colorado: integration of geological, stable-isotope, and fluid-inclusion evidence. Chem. Geol. 215, 281–315.
Bouvier, A., Vervoort, J.D., Patchett, P.J., 2008. The Lu–Hf and Sm–Nd isotopic composition of CHUR: constraints from unequilibrated chondrites and implications for the bulk composition of terrestrial planets. Earth Planet. Sci. Lett. 273, 48–57.
Chai, P., Sun, J.G., Xing, S.W., Men, L.J., Han, J.L., 2014. Early Cretaceous arc magmatism and high-sulphidation epithermal porphyry Cu–Au mineralization in Yanbian area, Northeast China: the Duhuangling example. Int. Geol. Rev. 57, 1267–1293.
Chang, Z.S., Hedenquist, J.W., White, N.C., Cooke, D.R., Roach, M., Deyell, C.L., Garcia, J., Gemmell, J.B., McKnight, S., Cuison, A.L., 2011. Exploration tools for linked porphyry and epithermal deposits: example from the Mankayan intrusion-centered Cu–Au District, Luzon, Philippines. Econ. Geol. 106, 1365–1398.
Chen, H.A., Zhu, X.P., Ma, D.F., Huang, H.X., Li, G.M., Li, Y.B., Li, Y.C., Wei, L.J., Liu, C.Q., 2013. Geochronology and geochemistry of the Bolong porphyry Cu–Au deposit, Tibet and its mineralizing significance. Acta Geol. Sin. 87, 1593–1611 (in Chinese with English abstract).
Cooke, D.R., Deyell, C.L., Waters, P.J., Gonzales, R.I., Zaw, K., 2011. Evidence for magmatic–hydrothermal fluids and ore-forming processes in epithermal and porphyry deposits of the Baguio district, Philippines. Econ. Geol. 106, 1399–1424.
Corfu, F., Hanchar, J.M., Hoskin, P.W.O., Kinny, P., 2003. Atlas of zircon textures. Rev. Mineral. Geochem. 53, 469–500.
Craddock, P.R., Dauphas, N., 2011. Iron isotopic compositions of geological reference materials and chondrites. Geostand. Geoanal. Res. 35, 101–123.
Driesner, T., Heinrich, C.A., 2007. The system $H_2O$–NaCl. Part I: correlation formulae for phase relations in temperature-pressure-composition space from 0 to 1000 °C, 0 to 5000 bar, and 0 to 1 $X_{NaCl}$. Geochim. Cosmochim. Acta 71, 4880–4901.
Einaudi, M.T., Hedenquist, J.W., Inan, E.E., 2003. Sulfidation state of fluids in active and extinct hydrothermal systems: transitions from porphyry to epithermal environments. Soc. Econ. Geol. Spec. Publ. 10, 285–313.
Foden, J., Sossi, P.A., Wawryk, C.M., 2015. Fe isotopes and the contrasting petrogenesis of A-, I- and S-type granite. Lithos 212, 32–44.
Fu, J.J., Zhao, Y.Y., Guo, S., 2014. Geochemical characteristics and significance of granodiorite porphyry in the Duolong ore concentration area, Tibet. Acta Petrol. Mineral. 33, 1039–1051 (in Chinese with English abstract).
Graham, S., Pearson, N., Jackson, S., Griffin, W., O'Reilly, S.Y., 2004. Tracing Cu and Fe from source to porphyry: in situ determination of Cu and Fe isotope ratios in sulfides from the Grasberg Cu–Au deposit. Chem. Geol. 207, 147–169.
Griffin, W.L., Pearson, N.J., Belousova, E., Jackson, S.E., van Achterbergh, E., O'Reilly, S.Y., Shee, S.R., 2000. The Hf isotope composition of cratonic mantle: LAM–MC–ICPMS analysis of zircon megacrysts in kimberlites. Geochim. Cosmochim. Acta 64, 133–147.
Griffin, W.L., Wang, X., Jackson, S.E., Pearson, N.J., O'Reilly, S.Y., Xu, X.S., Zhou, X.M., 2002. Zircon chemistry and magma mixing, SE China: in-situ analysis of Hf isotopes, Tonglu and Pingtan igneous complexes. Lithos 61, 237–269.
Hall, D.L., Sterner, S.M., Bodnar, R.J., 1988. Freezing point depression of NaCl–KCl–$H_2O$ solutions. Econ. Geol. 83, 197–202.
Hedenquist, J.W., Lowenstern, J.B., 1994. The role of magmas in the formation of hydrothermal ore deposits. Nature 370, 519–527.
Hedenquist, J.W., Arribas Jr., A., Gonzales-Urien, E., 2000. Exploration for epithermal gold deposits. Rev. Econ. Geol. 13, 245–277.
Hedenquist, J.W., Arribas, A., Reynolds, T.J., 1998. Evolution of an intrusion-centered hydrothermal system: far southeast-Lepanto porphyry and epithermal Cu–Au deposits, Philippines. Econ. Geol. 93, 373–404.
Heinrich, C.A., 2005. The physical and chemical evolution of low-salinity magmatic fluids at the porphyry to epithermal transition: a thermodynamic study. Mineral. Deposita 39, 864–889.
Heinrich, C.A., Driesner, T., Stefansson, A., Seward, T.M., 2004. Magmatic vapor contraction and the transport of gold from the porphyry environment to epithermal ore deposits. Geology 32, 761–764.
Hildreth, W., Moorbath, S., 1988. Crustal contributions to arc magmatismin the Andes of Central Chile. Contrib. Mineral. Petrol. 98, 455–489.
Huang, F., Zhang, Z., Lundstrom, C.C., Zhi, X., 2011. Iron and magnesium isotopic compositions of peridotite xenoliths from Eastern China. Geochim. Cosmochim. Acta 75, 3318–3334.
Hou, Z.Q., Gao, Y.F., Qu, X.M., Rui, Z.Y., Mo, X.X., 2004. Origin of adakitic intrusives generated during mid-Miocene east-west extension in southern Tibet. Earth Planet. Sci. Lett. 220, 139–155.
Hou, Z.Q., Ma, H.W., Zaw, K., Zhang, Y.Q., Wang, M.J., Wang, Z., Pan, G.T., Tang, R.L., 2003. The Himalayan Yulong porphyry copper belt: product of large-scale strike-slip faulting in eastern Tibet. Econ. Geol. 98 (1), 125–145.
Imai, A., Listanco, E.L., Fujii, T., 1993. Petrologic and sulfur isotopic significance of highly oxidized and sulfur-rich magma of Mt-Pinatubo, Philippines. Geology 21, 699–702.
Jackson, S.E., Pearson, N.J., Griffin, W.L., Belousova, E.A., 2004. The application of laser ablation-inductively coupled plasma-mass spectrometry to in situ U–Pb zircon geochronology. Chem. Geol. 211, 47–69.
Kapp, P., Yin, A., Harrison, T.M., Ding, L., 2005. Cretaceous–Tertiary shortening, basin development, and volcanism in central Tibet. Geol. Soc. Am. Bull. 117 (7-8), 865–878.
Kennedy, A.K., Wotzlaw, J.F., Schaltegger, U., Crowley, J.L., Schmitz, M., 2014. Eocene zircon reference material for microanalysis of U–Th–Pb isotopes and trace elements. Can. Mineral. 52, 409–421.
Li, J.X., 2008. Geochronology, Petrology And Metallogeneses Of High Oxidized Magma–Hydrothermal Fluid Of Duobuza Gold-Rich Porphyry Copper Deposit In Bangonghu Belt, Northern Tibet (Ph.D thesis) Institute of Geology and Geophysics, Chinese Academy of Sciences, p. 225 (in Chinese with English abstract).
Li, J.X., Qin, K.Z., Li, G.M., Zhao, J.X., Cao, M.J., 2015a. Petrogenesis of diabase from accretionary prism in the southern Qiangtang terrane, central Tibet: evidence from U–Pb geochronology, petrochemistry and Sr–Nd–Hf–O isotope characteristics. Island Arc 24 (2), 232–244.
Li, G.M., Zhang, X.N., Qin, K.Z., Sun, X.G., Zhao, J.X., Yin, X.B., Li, J.X., Yuan, H.S., 2015b. The telescoped porphyry-high sulfidation epithermal Cu (–Au) mineralization of Rongna deposit in Duolong ore cluster at the southern margin of Qiangtang Terrane, Central Tibet: integrated evidence from geology, hydrothermal alteration and sulfide assemblages. Acta Petrol. Sin. 31, 2307–2324 (in Chinese with English abstract).
Li, G.M., Li, J.X., Qin, K.Z., Duo, J., Zhang, T.P., Xiao, B., Zhao, J.X., 2012. Geology and hydrothermal alteration of the Duobuza gold-rich Porphyry copper district in the Bangongco metallogenetic belt, Northwestern Tibet. Resour. Geol. 62, 99–118.
Li, J.X., Li, G.M., Qin, K.Z., Xiao, B., 2011a. High-temperature magmatic fluid exsolved from magma at the Duobuza porphyry copper-gold deposit, Northern Tibet. Geofluids 11, 134–143.
Li, J.X., Qin, K.Z., Li, G.M., Xiao, B., Zhao, J.X., Chen, L., 2011b. Magmatic–hydrothermal evolution of the Cretaceous Duolong gold-rich porphyry copper deposit in the Bangongco metallogenic belt, Tibet: evidence from U–Pb and $^{40}Ar/^{39}Ar$ geochronology. J. Asian Earth Sci. 41, 525–536.
Li, G.M., Li, J.X., Qin, K.Z., Zhang, T.P., Xiao, B., 2007. High temperature, salinity and strong oxidation ore-forming fluid at Duobuza gold-rich porphyry copper deposit in the Bangonghu tectonic belt, Tibet: evidence from fluid inclusions. Acta Petrol. Sin. 23, 935–952 (in Chinese with English abstract).
Li, J.X., Qin, K.Z., Li, G.M., Richards, J.P., Zhao, J.X., Cao, M.J., 2014. Geochronology, geochemistry, and zircon Hf isotopic compositions of Mesozoic intermediate-felsic intrusions in central Tibet: Petrogenetic and tectonic implications. Lithos 198, 77–91.
Li, J.X., Qin, K.Z., Li, G.M., Xiao, B., Zhao, J.X., Cao, M.J., Chen, L., 2013. Petrogenesis of ore-bearing porphyries from the Duolong porphyry Cu–Au deposit, central Tibet:

evidence from U–Pb geochronology, petrochemistry and Sr–Nd–Hf–O isotope characteristics. Lithos 160, 216–227.
Li, J.X., Qin, K.Z., Li, G.M., Xiao, B., Zhao, J.X., Chen, L., 2016. Petrogenesis of Cretaceous igneous rocks from the Duolong porphyry Cu–Au deposit, central Tibet: evidence from zircon U–Pb geochronology, petrochemistry and Sr–Nd–Pb–Hf isotope characteristics. Geol. J. 51 (2), 285–307.
Liu, S., Hu, R.Z., Gao, S., Feng, C.X., Coulson, I.M., Feng, G.Y., Qi, Y.Q., Yang, Y.H., Yang, C.G., Tang, L., 2012. U–Pb zircon age, geochemical and Sr–Nd isotopic data as constraints on the petrogenesis and emplacement time of andesites from Gerze, southern Qiangtang Block, northern Tibet. J. Asian Earth Sci. 45, 150–161.
Liu, D.L., Huang, Q.S., Fan, S.Q., Zhang, L.Y., Shi, R.D., Ding, L., 2014. Subduction of the Bangong–Nujiang Ocean: constraints from granites in the Bangong Co area, Tibet. Geol. J. 49, 188–206.
Ludwig, K.R., 2003. ISOPLOT 3.0: a geochronological toolkit for Microsoft excel. Berkeley Geochronology Center, Special Publication, pp. 1–71.
Matsuhisa, Y., Goldsmith, J.R., Clayton, R.N., 1979. Oxygen isotopic fractionation in the system quartz–albite–anorthite–water. Geochim. Cosmochim. Acta 43, 1131–1140.
Morel, M.L.A., Nebel, O., Nebel-Jacobsen, Y.J., Miller, J.S., Vroon, P.Z., 2008. Hafnium isotope characterization of the GJ-1 zircon reference material by solution and laser-ablation MC–ICPMS. Chem. Geol. 255, 231–235.
Muntean, J.L., Einaudi, M.T., 2001. Porphyry–epithermal transition: maricunga belt, northern Chile. Econ. Geol. 96 (4), 743–772.
Ohmoto, H., Rye, R.O., 1979. Isotopes of sulfur and carbon. In: Barnes, H.L. (Ed.), Geochemistry of Hydrothermal Ore Deposits, second ed. Wiley, New York, pp. 509–567.
Pan, G.T., Wang, L.Q., Li, R.S., Yuan, S.H., Ji, W.H., Yin, F.G., Zhang, W.P., Wang, B.D., 2012. Tectonic evolution of the Qinghai–Tibet Plateau. J. Asian Earth Sci. 53, 3–14.
Polyakov, V.B., Soultanov, D.M., 2011. New data on equilibrium iron isotope fractionation among sulfides: constraints on mechanisms of sulfide formation in hydrothermal and igneous systems. Geochim. Cosmochim. Acta 75, 1957–1974.
Pudack, C., Halter, W.E., Heinrich, C.A., Pettke, T., 2009. Evolution of magmatic vapor to gold-rich epithermal liquid: The porphyry to epithermal transition at Nevados de Famatina, Northwest Argentina. Econ. Geol. 104, 449–477.
Richards, J.P., 2011. Magmatic to hydrothermal metal fluxes in convergent and collided margins. Ore Geol. Rev. 40, 1–26.
Roedder, E., 1984. Fluid inclusions. Rev. Mineral. 12, 1–644.
Rye, R.O., 1993. The evolution of magmatic fluids in the epithermal environment: the stable isotope perspective. Econ. Geol. 88, 733–753.
Rye, R.O., 2005. A review of the stable-isotope geochemistry of sulfate minerals in selected igneous environments and related hydrothermal systems. Chem. Geol. 215, 5–36.
Schauble, E.A., 2004. Applying stable isotope fractionation theory to new systems. Rev. Mineral. Geochem. 55, 65–111.
Seal, R.R., 2006. Sulfur isotope geochemistry of sulfide minerals. Rev. Mineral. Geochem. 61, 633–677.
She, H.Q., Li, J.W., Ma, D.F., Li, G.M., Zhang, D.Q., Feng, C.Y., Qu, W.J., Pan, G.T., 2009. Molybdenite Re–Os and SHRIMP zircon U–Pb dating of Duobuza porphyry copper deposit in Tibet and its geological implications. Mineral Deposits 28, 737–746 (in Chinese with English abstract).
Shi, R.D., 2007. SHRIMP dating of the Bangong Lake SSZ-type ophiolite: constraints on the closure time of ocean in the Bangong Lake–Nujiang River, northwestern Tibet. Chin. Sci. Bull. 52 (7), 936–941.
Sillitoe, R.H., 2010. Porphyry copper systems. Econ. Geol. 105, 3–41.
Slama, J., Kosler, J., Condon, D.J., Crowley, J.L., Gerdes, A., Hanchar, J.M., Horstwood, M.S.A., Morris, G.A., Nasdala, L., Norberg, N., Schaltegger, U., Schoene, B., Tubrett, M.N., Whitehouse, M.J., 2008. Plesovice zircon — a new natural reference material for U–Pb and Hf isotopic microanalysis. Chem. Geol. 249, 1–35.
Sterner, S.M., Hall, D.L., Bodnar, R.J., 1988. Synthetic fluid inclusions. V. Solubility relations in the system NaCl–KCl–$H_2O$ under vapour-saturated conditions. Geochim. Cosmochim. Acta 52, 989–1005.
Syverson, D.D., Borrok, D.M., Seyfried, W.E., 2013. Experimental determination of equilibrium Fe isotopic fractionation between pyrite and dissolved Fe under hydrothermal conditions. Geochim. Cosmochim. Acta 122, 170–183.
Vennemann, T.W., Muntean, J.L., Kesler, S.E., Oneil, J.R., Valley, J.W., Russell, N., 1993. Stable isotope evidence for magmatic fluids in the Pueblo Viejo epithermal acid sulfate Au–Ag Deposit, Dominican-Republic. Econ. Geol. 88, 55–71.
Vervoort, J.D., Blichert-Toft, J., 1999. Evolution of the depleted mantle: Hf isotope evidence from juvenile rocks through time. Geochim. Cosmochim. Acta 63, 533–556.
Wang, Y., Zhu, X.K., Cheng, Y.B., 2015. Fe isotope behaviours during sulfide-dominated skarn-type mineralisation. J. Asian Earth Sci. 103, 374–392.
Wawryk, C.M., Foden, J.D., 2015. Fe-isotope fractionation in magmatic–hydrothermal mineral deposits: a case study from the Renison Sn–W deposit, Tasmania. Geochim. Cosmochim. Acta 150, 285–298.
Wiedenbeck, M., Alle, P., Corfu, F., Griffin, W.L., Meier, M., Oberli, F., Vonquadt, A., Roddick, J.C., Speigel, W., 1995. Three natural zircon standards for U–Th–Pb, Lu–Hf, trace-element and ree analyses. Geostand. Newslett. 19, 1–23.
Wu, F.Y., Yang, Y.H., Xie, L.W., Yang, J.H., Xu, P., 2006. Hf isotopic compositions of the standard zircons and baddeleyites used in U–Pb geochronology. Chem. Geol. 234, 105–126.
Xiao, J.B., 2012. Genesis Of The Duobuza Copper Deposit In The Western Bangong–Nujiang Metallogenic Belt, Tibet (Master thesis) Chengdu University of Technology, p. 59 (in Chinese with English abstract).
Xie, L.W., Zhang, Y.B., Zhang, H.H., Sun, J.F., Wu, F.Y., 2008. In situ simultaneous determination of trace elements, U–Pb and Lu–Hf isotopes in zircon and baddeleyite. Chin. Sci. Bull. 53, 1565–1573.
Yin, A., Harrison, T.M., 2000. Geologic evolution of the Himalayan–Tibetan orogen. Annu. Rev. Earth Planet. Sci. 28, 211–280.
Zhang, Z., Geng, Q.R., Peng, Z.M., Cong, F., Guan, J.L., 2011. Geochemistry and geochronology of the Caima granites in the western part of the Bangong Lake–Nujiang metallogenic zone, Xizang. Sediment. Geol. Tethyan Geol. 31 (4), 86–96 (in Chinese with English abstract).
Zhang, K.J., Zhang, Y.X., Tang, X.C., Xia, B., 2012. Late Mesozoic tectonic evolution and growth of the Tibetan plateau prior to the Indo-Asian collision. Earth Sci. Rev. 114 (3-4), 236–249.
Zhao, X.M., Zhang, H.F., Zhu, X.K., Zhu, B., Cao, H.H., 2015. Effects of melt percolation on iron isotopic variation in peridotites from Yangyuan, North China Craton. Chem. Geol. 401, 96–110.
Zhou, J.S., Meng, X.J., Zang, W.S., Yang, Z.S., Xu, Y.T., Zhang, X., 2013. Zircon U–Pb geochronologyand trace element geochemistry of the ore-bearing porphyry in Qingcaoshanporphyry Cu–Au deposit, Tibet, and its geological significance. Chem. Geol. 29, 3755–3766 (in Chinese with English abstract).
Zhu, X.P., Chen, H.A., Liu, H.F., Ma, D.F., Li, G.M., Huang, H.X., Zhang, H., Liu, C.Q., Wei, L.J., 2015a. Zircon U–Pb ages, geochemistry of the porphyries from the Duobuza porphyry Cu–Au deposit, Tibet and their metallogenic significance. Acta Geol. Sin. 89, 534–548 (in Chinese with English abstract).
Zhu, X.P., Li, G.M., Chen, H.A., Ma, D.F., Huang, H.X., 2015b. Zircon U–Pb, molybdenite Re–Os and K-feldspar $^{40}Ar/^{39}Ar$ dating of the Bolong porphyry Cu–Au deposit, Tibet, China. Resour. Geol. 65, 122–135.
Zhu, X.P., Chen, H.A., Ma, D.F., Huang, H.X., Li, G.M., Liu, C.Q., Wei, L.J., 2012. $^{40}Ar/^{39}Ar$ dating for K-feldspar from Duobuza porphyry copper–gold deposit in Tibet, China and its geological significance. Geoscience 26, 656–662 (in Chinese with English abstract).
Zhu, D.C., Zhao, Z.D., Niu, Y.L., Dilek, Y., Hou, Z.Q., Mo, X.X., 2013. The origin and pre-Cenozoic evolution of the Tibetan Plateau. Gondwana Res. 23 (4), 1429–1454.